

Fractional neural attention for efficient multiscale sequence processing

Cheng Kevin Qu,* Andrew Ly,* and Pulin Gong[†]
School of Physics, University of Sydney, Sydney, NSW, Australia

Attention mechanisms underpin the computational power of Transformer models, which have achieved remarkable success across diverse domains. Yet understanding and extending the principles underlying self-attention remains a key challenge for advancing artificial intelligence. Drawing inspiration from the multiscale dynamics of biological attention and from dynamical systems theory, we introduce Fractional Neural Attention (FNA), a principled, neuroscience-inspired framework for multiscale information processing. FNA models token interactions through Lévy diffusion governed by the fractional Laplacian, intrinsically realizing simultaneous short- and long-range dependencies across multiple scales. This mechanism yields greater expressivity and faster information mixing, advancing the foundational capacity of Transformers. Theoretically, we show that FNA’s dynamics are governed by the fractional diffusion equation, and that the resulting attention networks exhibit larger spectral gaps and shorter path lengths—mechanistic signatures of enhanced computational efficiency. Empirically, FNA achieves competitive text-classification performance even with a single layer and a single head; it also improves performance in image processing and neural machine translation. Finally, the diffusion map algorithm from geometric harmonics enables dimensionality reduction of FNA weights while preserving the intrinsic structure of embeddings and hidden states. Together, these results establish FNA as a principled mechanism connecting self-attention, stochastic dynamics, and geometry, providing an interpretable, biologically grounded foundation for powerful, neuroscience-inspired AI.

Transformers [1] have delivered striking results on sequential data, spanning natural language [2, 3] and time series [4, 5], and have been successfully adapted to vision [6] and graph learning [7]. Their pervasive success is widely attributed to the self-attention mechanism that models the relationship between tokens. Yet the principles that make self-attention effective remain largely unclear. Recent studies have recast token embeddings as spatial variables and layers as a time coordinate, yielding a continuous-time view of the limiting dynamics of self-attention [8, 9]. Notably, a bistochastic formulation of self-attention reduces to classical Brownian diffusion [9]. Furthermore, local-global hybrids of attention have been found to consistently improve long-sequence processing [10, 11]. This two-scale structure has largely been engineered through *ad hoc* manipulation of sparsification windows, combining sliding windows with special global tokens or random links. A principled formulation of self-attention that inherently entails multiscale dynamics has been missing.

Neuroscience offers an instructive perspective. It has been shown that attentional “spotlights” exhibit local shifts interspersed with long-range jumps, with step sizes following heavy-tailed, power-law statistics [12] (Fig. 1). These attention-sampling dynamics unfold across multiple, nested scales, and are well-characterized as fractional Lévy processes. Such properties account for diverse neurophysiological observations of attention sampling [12] and confer computational advantages [13], enabling flexible sampling of complex sensory scenes such as natural environments rich in salient features. In contrast, Brownian-motion-based sampling is predominantly local (Fig. 1), due to the lack of long jumps. Although neuroscience-inspired artificial intelligence (NeuroAI) is widely expected to be crucial for future advances [14, 15], a neurally grounded

attention rule that operationalizes realistic, multiscale computation within Transformer architectures remains unexplored.

In this study, we introduce a neuroscience-inspired attention mechanism, which we term fractional neural attention (FNA), that integrates Lévy diffusion into self-attention through a dynamical-systems formulation. FNA intrinsically realizes simultaneous short- and long-range interactions among tokens across multiple scales, yielding greater expressivity and faster information mixing, thus advancing the foundational capacity of Transformers beyond efficiency-oriented designs. To elucidate the theoretical framework of FNA, we first prove that FNA’s second-order dynamics are governed by the fractional Laplacian (Fig. 1) [16], a scale-free pseudo-differential operator of order $\alpha \in [1, 2]$ that is the infinitesimal generator of Lévy processes [17]. This yields an interpretable, geometry-aware account of attention as diffusion on a manifold, enabling the canonical use of diffusion maps for dimensionality reduction to obtain meaningful representations of the attention weights [18, 19]. The parameter α controls locality versus non-locality, recovering the local Brownian limit at $\alpha = 2$ and inducing power-law tails for $\alpha < 2$ that support multiscale (i.e., scale-free) interactions among tokens in embedding space.

We then explain FNA’s computational advantages using a network-theoretic analysis of the induced attention networks. Relative to standard self-attention, FNA produces larger spectral gaps and shorter path lengths, enabling faster information mixing and greater representational capacity. This analysis explains why FNA attains strong performance with substantially fewer layers—sometimes a single layer—than conventional Transformers. Finally, across text (IMDb), vision (CIFAR-10 with ViTs [6]) and machine translation (Multi30K En-De [20]), multiscale FNA matches or exceeds strong Transformer baselines. Together, these results establish a principled, multiscale attention mechanism that connects insights from neuroscience and dynamical systems to advance AI.

* These authors contributed equally to this work.

[†] pulin.gong@sydney.edu.au

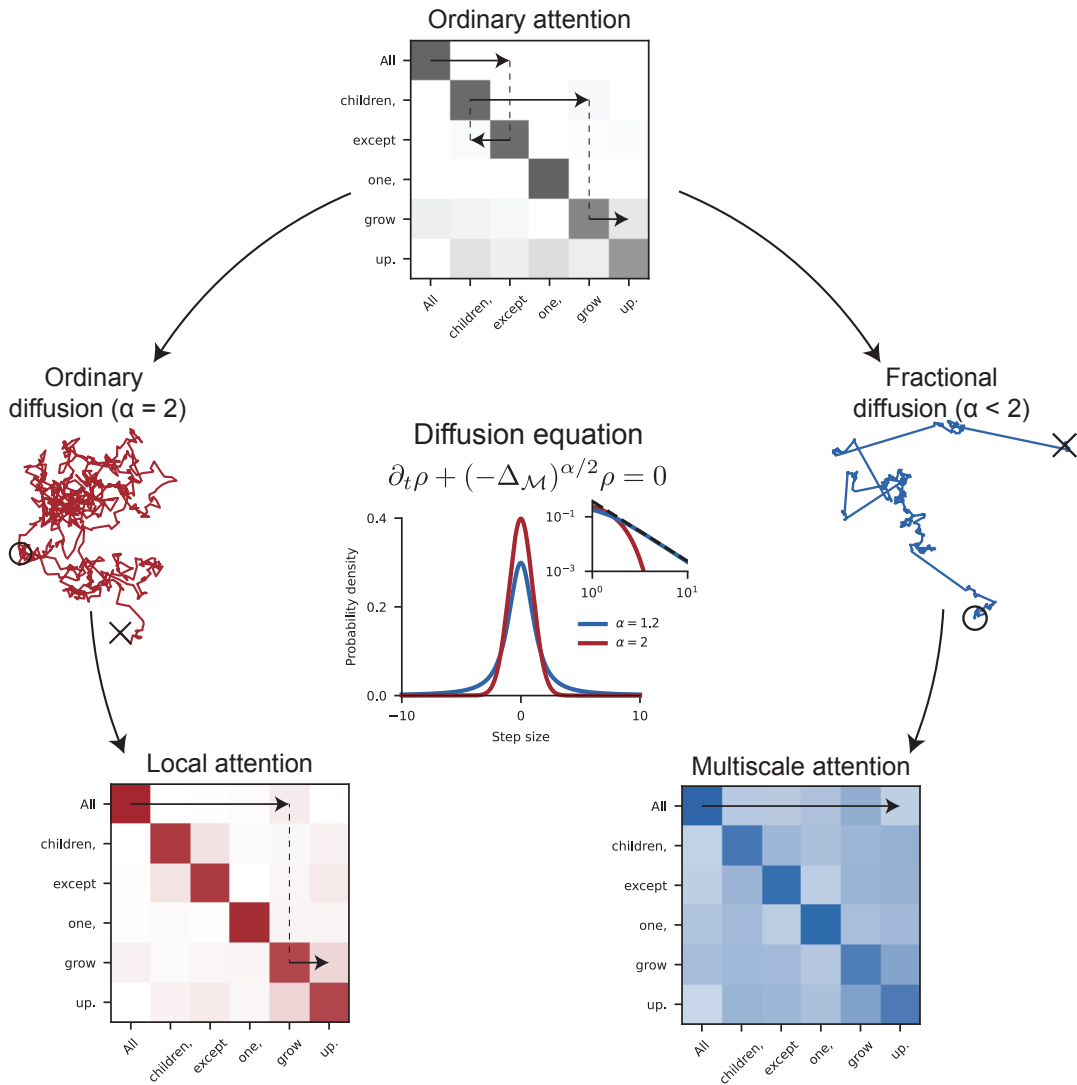


Fig. 1. From fractional diffusion to attention. The fractional diffusion equation describes the density evolution of Lévy processes for $\alpha < 2$. When $\alpha = 2$, it reduces to the classical diffusion equation corresponding to Brownian motion. The associated step-size distributions are heavy-tailed (i.e., multiscale) for $\alpha < 2$ and Gaussian for $\alpha = 2$. Inspired by the role of fractional diffusion in neurobiological attention [12], we incorporate these dynamics into Transformer self-attention to obtain fractional neural attention (FNA). Multiscale FNA ($\alpha < 2$) enhances the expressivity of attention, enabling the first word of a sentence (e.g., “All children, except one, grow up.”—Peter Pan) to attend to the last with a single “step” of the attention mechanism. In contrast, local attention ($\alpha = 2$) and standard attention typically require multiple steps. Steps are represented by arrows within the attention matrices.

THEORETICAL FRAMEWORK OF FRACTIONAL NEURAL ATTENTION (FNA)

We develop a theoretical framework for FNA through three steps: First, we dissect the self-attention mechanism of the vanilla Transformer as a continuous-time dynamical system, uncovering a fundamental connection to local diffusive behavior. Second, we generalize this to non-local, fractional diffusion by exploiting the fractional Laplacian operator, the infinitesimal generator of the symmetric α -stable Lévy processes. Third, we integrate this fractional diffusion into attention to formulate FNA.

Self-attention as a dynamical system.

The original Transformer model employs self-attention in a feed-forward manner as the key structure for information processing [1, 21, 22]. To summarize, the self-attention block in the $(l + 1)^{\text{th}}$ layer receives as input a sequence of n tokens embedded in a manifold such as Euclidean space, i.e., $\mathbf{X} := (\mathbf{x}_1^l, \mathbf{x}_2^l, \dots, \mathbf{x}_n^l) \in \mathbb{R}^{d \times n}$ where $\mathbf{x}_i^l \in \mathbb{R}^d$ for each i . It projects these embedding vectors to queries, keys and values via $\mathbf{q} = \mathbf{W}_Q \mathbf{x}$, $\mathbf{k} = \mathbf{W}_K \mathbf{x}$ and $\mathbf{v} = \mathbf{W}_V \mathbf{x}$, respectively, where $\mathbf{W}_Q, \mathbf{W}_K \in \mathbb{R}^{d_k \times d}$ and $\mathbf{W}_V \in \mathbb{R}^{d_v \times d}$ are learnable projection matrices. The self-attention block updates each token representation by aggregating information across the entire input

sequence, producing the output embedding: [9, 23–25]:

$$\mathbf{x}_i^{l+1} = \mathbf{x}_i^l + \sum_{j=1}^n A_{ij} \mathbf{W}_V \mathbf{x}_j^l, \quad (1)$$

where $\mathbf{A} = \text{softmax}(\mathbf{C}) := N_R(\exp[\mathbf{C}]) \in \mathbb{R}^{n \times n}$. The exponential function $\exp[\cdot]$ is applied element-wise to the similarity matrix $\mathbf{C} \in \mathbb{R}^{n \times n}$, whose entries are calculated as query-key dot products $C_{ij} := \mathbf{q}_i^\top \mathbf{k}_j = \mathbf{x}_i^\top \mathbf{W}_Q^\top \mathbf{W}_K \mathbf{x}_j$, and $N_R(\cdot)$ denotes row normalization. The resulting attention weight matrix \mathbf{A} is right-stochastic: each row sums to 1, and each entry A_{ij} can be interpreted as the normalized weight assigned by the i^{th} query to the j^{th} key, applied to value $\mathbf{v}_j := \mathbf{W}_V \mathbf{x}_j$ when forming \mathbf{x}_i^{l+1} . In other words, the attention weights encode single-step transition probabilities over the token sequence. For notational convenience, we collect queries, key and values into matrices $\mathbf{Q} := (\mathbf{q}_1, \dots, \mathbf{q}_n)$, $\mathbf{K} := (\mathbf{k}_1, \dots, \mathbf{k}_n)$ and $\mathbf{V} := (\mathbf{v}_1, \dots, \mathbf{v}_n)$, respectively. In addition to the self-attention mechanism, the residual connections are a crucial component of the Transformer architecture. They prevent representational degradation within the attention block; without them, the model output suffers from rank-collapse at a double-exponential rate with respect to depth [26]. To guarantee the well-definedness of equation 1, we assume $d_k = d_v = d$ [1].

Following recent studies [8, 9, 25], we now interpret the self-attention mechanism as a dynamical system. The residual form of equation 1 corresponds to an Euler discretization with step-size 1 of the ordinary differential equation (ODE)

$$\dot{\mathbf{x}}_i(t) = T(\mathbf{x}_i(t)) \text{ for all } i, \quad (2)$$

where the token embedding \mathbf{x}_i is treated as spatial variable and the layer l in equation 1 is viewed as a time variable. This continuous-time perspective parallels formulations in the framework of neural ODEs [27]. Thus, we replace l with t to highlight this interpretation. Furthermore, we construct the push-forward map T as

$$T_{\mu,t}(\mathbf{x}) = \frac{1}{t} \int_{\mathbb{R}^d} k_t^{\text{SA}}(\mathbf{x}, \mathbf{x}') \mathbf{W}_V \mathbf{x}' d\mu(\mathbf{x}'). \quad (3)$$

The superscript SA represents self-attention and $k_t^{\text{SA}}(\mathbf{x}, \mathbf{x}') := \frac{\exp(\mathbf{x}^\top \mathbf{W}_Q^\top \mathbf{W}_K \mathbf{x}' / t)}{\int_{\mathbb{R}^d} \exp(\mathbf{x}^\top \mathbf{W}_Q^\top \mathbf{W}_K \mathbf{x}' / t) d\mu(\mathbf{x}')}$ is the associated attention kernel; t corresponds to time and μ is the distribution of the token embeddings. Each token \mathbf{x}_i can be viewed as a particle whose position evolves according to equation 2. We thus use the terms ‘token’ and ‘particle’ interchangeably throughout the remainder of the text [8]. Implicitly, we take the infinite particle limit $n \rightarrow \infty$ to obtain the integral expression of the summation term in equation 1. The map T depends on $\mu \in \mathcal{P}(\mathbb{R}^d)$, the probability measure supported on \mathbb{R}^d from which the embeddings \mathbf{x}' are sampled, which can be identified with a density function ρ of the particle positions: $d\mu(\mathbf{x}) = \rho(\mathbf{x}) d\mathbf{x}$. Taking the limit $t \rightarrow 0$, which physically represents an infinitesimal step-size, allows the ODE (equation 2) to be written as a continuity equation describing the second-order dynamics:

$$\partial_t \mu + \text{div}(\bar{T}_\mu) = 0, \quad (t, \mathbf{x}) \in \mathbb{R}^+ \times \mathbb{R}^d \quad (4)$$

where $\bar{T}_\mu := T_{\mu,0}$. This result is obtained by replacing the dot-product between the queries and keys in k_t^{SA} with their squared Euclidean distance in equation 3 [9, 28]. Upon setting $t = 1$ and $\mu := \frac{1}{n} \delta_{\mathbf{x}_i(0)}$ in equation 3, the original self-attention update (equation 1) can be recovered through the Euler discretization of equation 2 due to the permutation-equivariance of self-attention [23, 24, 29].

The continuity equation provides a deeper understanding of how the probability measure over particles evolves. For instance, a recent work studied a bistochastic form of self-attention, in which an iterative scheme of column and row normalizations is applied to the attention matrix \mathbf{A} [9]. Under this construction and certain conditions on the projection matrices (i.e., $\mathbf{W}_K^\top \mathbf{W}_Q = \mathbf{W}_Q^\top \mathbf{W}_K = -\mathbf{W}_V$), equation 4 reduces to the spatially local diffusion equation:

$$\partial_t \rho - \Delta \rho = 0, \quad (5)$$

where Δ is the standard Laplacian operator and $\rho := \rho(t, \mathbf{x}) \in \mathbb{R}^+ \times \mathbb{R}^d$ is the particle density. With modern deep models such as GPT-3, employing up to 96 layers [30], understanding the layer-wise (continuum) limit of self-attention in equation 1 becomes increasingly important. Adopting a dynamical-systems perspective clarifies how the probability measure governing the particles evolves across layers. Within this framework, we show that self-attention naturally admits a fractional diffusion formulation.

Fractional diffusion.

We now establish the spatially fractional generalization of the diffusion equation in order to guide its integration within self-attention. The generalization of equation 5 is the fractional diffusion equation on a Riemannian manifold \mathcal{M} :

$$\partial_t \rho + (-\Delta_{\mathcal{M}})^{\alpha/2} \rho = 0, \quad (6)$$

where the fractional Laplacian $(-\Delta_{\mathcal{M}})^{\alpha/2}$ is a non-local, pseudo-differential operator, $\alpha \in (0, d_{\mathcal{M}} + 1]$ is its fractional order and $d_{\mathcal{M}}$ is the dimension of the manifold \mathcal{M} . There are several equivalent definitions of the fractional Laplacian [16, 31]. In particular, for $\mathcal{M} = \mathbb{R}^d$, the fractional Laplacian can be defined as a singular integral:

$$(-\Delta)^{\alpha/2} u(\mathbf{x}) = c_{d,\alpha} \lim_{\varepsilon \downarrow 0} \int_{\mathbb{R}^d \setminus B(\mathbf{x}, \varepsilon)} \frac{u(\mathbf{x}) - u(\mathbf{y})}{\|\mathbf{x} - \mathbf{y}\|^{d+\alpha}} d\mathbf{y}, \quad (7)$$

where $\Delta := \Delta_{\mathbb{R}^d}$, $c_{d,\alpha} := \frac{\alpha 2^{\alpha-1} \Gamma(\frac{d+\alpha}{2})}{\pi^{d/2} \Gamma(1-\alpha/2)}$ is a normalization constant, Γ is the Gamma function and $B(\mathbf{x}, \varepsilon)$ is the open ball of radius ε centered at \mathbf{x} . When $\alpha \in [2, d_{\mathcal{M}} + 1]$, the operator reduces to the standard (local) Laplacian: the value of $\Delta f(x)$ depends only on an arbitrarily small neighborhood of f around x . In contrast, for $\alpha \in (0, 2)$, the value of the fractional Laplacian $(-\Delta)^{\alpha/2} f(x)$ depends on the entire domain according to the power-law weighting in the integral of equation 7. See ‘‘Methods’’ for a spectral definition of the fractional Laplacian for closed and compact manifolds.

The solution to the fractional diffusion equation is the isotropic α -scale invariant heat kernel $k_t(\mathbf{x}, \mathbf{y})$. The heat kernel depends on the geodesic distance $d_g(\cdot, \cdot)$ on the manifold \mathcal{M}

(see equation 21 in “Methods”) and is asymptotically bounded by:

$$\frac{c_1}{t^{d/\alpha}} \Phi\left(C_1 \frac{d_g(\mathbf{x}, \mathbf{y})}{t^{1/\alpha}}\right) \leq k_t(\mathbf{x}, \mathbf{y}) \leq \frac{c_2}{t^{d/\alpha}} \Phi\left(C_2 \frac{d_g(\mathbf{x}, \mathbf{y})}{t^{1/\alpha}}\right), \quad (8)$$

where c_1, c_2, C_1, C_2 are all positive constants and the decay function $\Phi : [0, \infty) \rightarrow [0, \infty)$ is monotonically decreasing. Such heat kernels k exhibit a dichotomy [32]:

1. If $\alpha \in [2, d_M + 1]$, then k is local and its decay is bounded by the exponential

$$\Phi_\alpha(z) = \exp\left(-z^{\frac{\alpha}{\alpha-1}}\right); \quad (9)$$

or

2. If $\alpha \in (0, 2)$, then k is non-local and its decay is bounded by the power law

$$\Phi_\alpha(z) = (1 + z)^{-(d_M + \alpha)}. \quad (10)$$

Henceforth, we consider $\alpha \in [1, 2]$ and $M = \mathbb{R}^d$ where $d_g(\mathbf{x}, \mathbf{y}) = \|\mathbf{x} - \mathbf{y}\|$. See “Methods” for further details on the fractional Laplacian, its connection to the α -scale invariant heat kernel (equation 8) and its generalization to non-Euclidean manifolds.

We next exemplify the dichotomy of local and multiscale dynamics encompassed within the fractional diffusion equation. For $\alpha = 2$, where equation 5 becomes the classical diffusion equation, the solution is the well-known Gaussian heat kernel:

$$k_t(\mathbf{x}, \mathbf{y}) := \frac{1}{(4\pi t)^{d/2}} e^{-\frac{\|\mathbf{x} - \mathbf{y}\|^2}{4t}}, \quad (11)$$

which decays exponentially in the squared Euclidean distance. This describes the probability density associated with the classical Brownian motion (Fig. 1). In contrast, for $\alpha < 2$, the solution yields disparate characteristics. For example, it simplifies to the well-known Poisson kernel when $\alpha = 1$:

$$k_t(\mathbf{x}, \mathbf{y}) = \frac{\tilde{c}_d}{t^d} \left(1 + \frac{\|\mathbf{x} - \mathbf{y}\|}{t^2}\right)^{-\frac{d+1}{2}}, \quad (12)$$

where $\tilde{c}_d = \Gamma\left(\frac{d+1}{2}\right)/\pi^{(d+1)/2}$. Such power-law heat kernels describe the probability densities of symmetric α -stable ($S\alphaS$) Lévy processes (see “Methods”). The increments of Lévy processes exhibit an asymptotic power-law decay, so large jumps occur with far higher probability than under Brownian motion (Fig. 1). Such heavy-tailed dynamics are efficient for neural circuits implementing probabilistic computation [13] and for spatial-visual attention sampling [12]. They are also consistent with observed efficient search strategies in animal foraging [33, 34].

Fractional neural attention.

We implement FNA through the following steps:

1. For all pairs of tokens $\mathbf{x}_i, \mathbf{x}_j \in \mathbb{R}^d$ in the sequence, calculate the fractional attention score \tilde{C}_{ij} as

$$\tilde{C}_{ij} = \Phi_\alpha\left(\frac{\|\mathbf{W}_Q \mathbf{x}_i - \mathbf{W}_K \mathbf{x}_j\|}{\kappa}\right), \quad (13)$$

where Φ_α is given by equation 9 or 10 depending on α and κ is a distance scaling constant.

We emphasize a key change to conventional self-attention: To exploit Φ_α , we replace the dot-product between the queries and keys by their Euclidean (or L^2) distance. This operation decouples the attention score from the softmax’s implicit exponential form, which has a fixed scale, and enables power-law (scale free) attention when $\alpha < 2$. Distance-based self-attention has been previously proposed, primarily to establish Lipschitz continuity [35]; our construction extends this approach and recovers it as a special case when $\alpha = 2$.

2. Compute the output of the FNA block as

$$\text{FAttn}(\mathbf{X}) := \tilde{\mathbf{A}} \mathbf{V}^\top, \quad \tilde{\mathbf{A}} := N_R(\tilde{\mathbf{C}}), \quad (14)$$

where $\tilde{\mathbf{C}}$ is the matrix of attention scores (equation 13).

For $\alpha = 2$, we set $\kappa = \sqrt{d_H}$ where $d_H = d/H$, consistent with common practice [1]. For $\alpha < 2$, we use different κ due to the explicit dependence on d of the non-local kernel. We note that $d_M = d_H$ in equation 10 and α is specified prior to training as a hyperparameter. For further details regarding the implementation of FNA, see “Methods”. Note that L^2 -normalization can also be applied to the embeddings prior to the attention map, naturally injecting them onto \mathbb{S}^{d-1} (see Appendix A 1 for the setup and additional results in Fig. A1).

Operator limit of FNA.

We now demonstrate that FNA induces the desired multiscale Lévy dynamics by verifying that the infinitesimal generator of FNA converges to the fractional Laplacian. Paralleling the dynamical-systems formulation of ordinary attention (equation 3), the infinitesimal generator of FNA dynamics is

$$\mathcal{H}^{\text{FNA}}[f] := \lim_{t \rightarrow 0} \frac{T_{\mu, t}^{\text{FNA}}[f] - f}{t}, \quad (15)$$

where

$$T_{\mu, t}^{\text{FNA}}[f](\mathbf{x}) = \int_{\mathbb{R}^d} k_t^{\text{FNA}}(\mathbf{x}, \mathbf{y}) f(\mathbf{y}) \rho(\mathbf{y}) d\text{vol}_y \quad (16)$$

is the push-forward map and

$$k_t^{\text{FNA}}(\mathbf{x}, \mathbf{x}') := \frac{\Phi_\alpha(\|\mathbf{W}_Q \mathbf{x} - \mathbf{W}_K \mathbf{x}'\|/t^{1/\alpha})}{\int_{\mathbb{R}^d} \Phi_\alpha(\|\mathbf{W}_Q \mathbf{x} - \mathbf{W}_K \mathbf{y}\|/t^{1/\alpha}) \rho(\mathbf{y}) d\text{vol}_y} \quad (17)$$

is the FNA kernel. The connection between the infinitesimal generator \mathcal{H}^{FNA} and the fractional Laplacian $(-\Delta)^{\alpha/2}$ relies on the isometry of queries and keys (Theorem 2). The push-forward map (equation 16) represents the spatially continuous

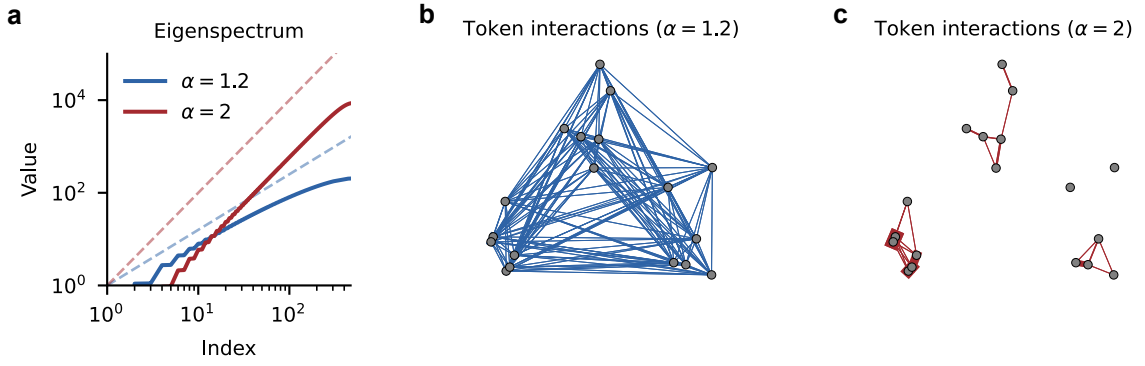


Fig. 2. FNA token interactions and spectral characteristics. **a** Solid lines show eigenvalues of the FNA attention weight matrix, ordered from small to large. Dashed lines represent eye guides with slopes of $j^{1.2}$ (blue) and j^2 (red) respectively where j corresponds to the eigenvalue index. **b** The gray-shaded circles represent the randomly sampled token embeddings. The thickness of the blue lines reflects the strength of the fractional attention weights, between connected queries and keys, scaled by a constant. Only connection strengths above 3.12×10^{-5} are presented. **c** Same as in **b** but for $\alpha = 2$ with the red lines representing the attention weight strengths.

analog of the FNA weights (equation 14) in the limit of $n \rightarrow \infty$ (see Appendix A 4). We proceed by showing how to guarantee these properties in the practical implementation of FNA.

Both the original attention [1] and our FNA apply linear projections of embedding vectors \mathbf{x} to obtain queries and keys: $\mathbf{q} = \iota_Q(\mathbf{x}) = \mathbf{W}_Q \mathbf{x}$ and $\mathbf{k} = \iota_K(\mathbf{x}) = \mathbf{W}_K \mathbf{x}$, respectively. For arbitrary \mathbf{W} , the projection ι is generally not an isometry because the geodesic distance between an arbitrary pair of tokens is not necessarily preserved. For $\mathcal{M} = \mathbb{R}^d$, an isometric projection ι can be realized under the following assumptions:

Assumption 1 (orthogonality): Assume single-head attention $H = 1$ and orthogonal query and key projection matrices $\mathbf{W}_{Q,K} \in O(d)$. The orthogonality of a weight matrix can be enforced during training through constrained optimization methods for matrix manifolds [36]. This condition has also been used in other Transformer architectures to maintain the token embedding manifold structure and thus preserve the injectivity of the model input-output map [37].

Assumption 2 (symmetry): Assume weight-tying between the queries and keys ($\mathbf{Q} = \mathbf{K}$, or equivalently $\mathbf{W}_Q = \mathbf{W}_K$). This condition has motivated the development of new architectures by linking the attention kernel k^{SA} to the Gaussian kernel in [38]. Weight-tying between $\mathbf{W}_{Q,K}$ in our case is needed only for the derivation of FNA’s fractional diffusion limit; it is not required for general FNA implementations. In recent studies [25], various assumptions on the keys and queries have been applied to understand self-attention, including $\mathbf{Q}^\top \mathbf{K} > 0$ (positive-definiteness) and $\mathbf{Q}^\top \mathbf{K} = \mathbf{I}$.

When both assumptions are satisfied, a meaningful parameter reduction of the original self-attention (equation 1) and FNA is possible through the following proposition (see “Methods” for proof).

Proposition 1. Assume $\mathcal{M} = \mathbb{R}^d$ or \mathbb{S}^{d-1} , single-head attention $H = 1$ and $\mathbf{W}_{Q,K} \in O(d)$ (i.e., Assumption 1). Then, self-attention (equation 1) and FNA (equation 13) with query and key projection matrices \mathbf{W}_Q and \mathbf{W}_K are equivalent to using an alternative pair of query/key projection matrices $\tilde{\mathbf{W}}_Q = \mathbf{I}$ and $\tilde{\mathbf{W}}_K = \mathbf{W}_Q^\top \mathbf{W}_K \in O(d)$. When Assumption 2 is further

satisfied, $\tilde{\mathbf{W}}_Q = \tilde{\mathbf{W}}_K = \mathbf{I}_d$.

Furthermore, the infinitesimal generator of FNA \mathcal{H}^{FNA} (equation 15) converges to the fractional Laplacian, resulting in multiscale Lévy dynamics, as shown in the following theorem:

Theorem 2 (PDE for FNA). *Let $\mu \in \mathcal{P}(\mathcal{M})$ be a probability measure supported on $\mathcal{M} = \mathbb{R}^d$ or \mathbb{S}^{d-1} with density $\rho \in C^3(\mathcal{M})$. Without loss of generality, set $\kappa = 1$. Under Assumptions 1 and 2, as $t \rightarrow 0$, the infinitesimal generator of FNA converges to the operator*

$$\mathcal{H}[f] = \frac{(-\Delta_{\mathcal{M}})^{\alpha/2}(f\rho) - f(-\Delta_{\mathcal{M}})^{\alpha/2}\rho}{\rho} \quad (18)$$

in L^2 . For a uniform grid on \mathcal{M} , $\mathcal{H}[f] = (-\Delta_{\mathcal{M}})^{\alpha/2}f$, recovering the fractional diffusion as in equation 6.

We outline the proof of Theorem 2 in “Methods”, drawing from the diffusion-maps framework [18, 39]. Under Assumptions 1 & 2, our FNA kernel (equation 17) satisfies the conditions of a rotation-invariant heat kernel (see “Methods”), allowing us to establish our proof. In the formulation, the infinitesimal generator of FNA (equation 18) depends on the underlying distribution of token embeddings ρ , which is generally non-uniform on the underlying manifold, i.e., $d\rho(\mathbf{x}) \neq \text{Vol}(\mathbb{S}^{d-1})^{-1}d\mathbf{x}$ for $\mathcal{M} = \mathbb{S}^{d-1}$ where the volume of the manifold constitutes the normalization factor $\text{Vol}(\mathbb{S}^{d-1}) := \int_{\mathbb{S}^{d-1}} d\text{vol}_{\mathbf{x}}$. We highlight this non-uniformity by visualizing empirical embedding distributions from several large pretrained models in Appendix A 2.

We next empirically verify the convergence of FNA to the fractional Laplacian by examining its eigenspectrum. The eigenspectrum is important because it uniquely distinguishes the standard and fractional Laplacian operators. For instance, Weyl’s law [40] states that the eigenvalues of the Laplace-Beltrami operator follow $\lambda_j \propto j^2$ for large j . In contrast, the eigenvalues of the fractional Laplacian operator theoretically follow $\lambda_j \propto j^\alpha$ for $\alpha < 2$ (see equation 22 in “Methods”). For

comparison, we calculate the empirical eigenvalues for FNA applied to 500 uniformly spaced points on \mathbb{S}^1 (see “Methods”). We find that the scaling of empirical eigenvalues agree with theoretical predictions for the operator limits in both $\alpha < 2$ (blue curves) and $\alpha = 2$ (red curves) regimes (Fig. 2a). We note that the discrepancy between theory and experiment increases with the eigenvalue magnitude. However, this can be mitigated by increasing the number of data points and reducing the bandwidth parameter ε where we set $\kappa = \sqrt{\varepsilon}$ in equation 13 (see “Methods”).

Furthermore, we confirm that FNA promotes multiscale interactions in the $\alpha < 2$ regime. To illustrate this, we impose Assumptions 1 and 2 on FNA (equation 13) with $\alpha = 1.2$ and 2, yielding $\mathbf{Q} = \mathbf{K} = \mathbf{X}$. The token embeddings (gray circles) $\mathbf{X} \in \mathbb{R}^{d \times n}$, where $(n, d) = (18, 2)$, are sampled from a two-dimensional multimodal distribution

$$\rho(\mathbf{x}) = \frac{1}{3} \sum_{i=1}^3 f_2(\mathbf{x}; \boldsymbol{\mu}_i, \boldsymbol{\Sigma})$$

consisting of two-dimensional Gaussian distributions $f_2(\mathbf{x}; \boldsymbol{\mu}, \boldsymbol{\Sigma})$ with three well-separated modes centered at $\boldsymbol{\mu}_1 = (3, 0)$, $\boldsymbol{\mu}_2 = (-3, 0)$ and $\boldsymbol{\mu}_3 = (0, \sqrt{3})$ respectively, and the covariance matrix $\boldsymbol{\Sigma} = \mathbf{I}/4$. We observe strong multiscale connectivity, including inter- and intra-cluster interactions, for $\alpha < 2$ (Fig. 2b). In contrast, $\alpha = 2$ exhibits intra-cluster connectivity only (Fig. 2c). Because of these distinct characteristics, we henceforth refer to the cases of $\alpha < 2$ and $\alpha = 2$ as multiscale FNA and local attention, respectively.

MECHANISMS OF FNA

In this section, we provide a mechanistic account of the computational advantages of FNA by comparing multiscale FNA ($\alpha < 2$), local attention ($\alpha = 2$) and vanilla dot-product attention (DP). We adopt a minimal modeling approach, widely used in theoretical deep-learning studies [8, 9, 23, 25, 41], and focus on single-head attention so that Assumptions 1 & 2 hold and the fractional-diffusion limit is exact. We then train all models on the IMDb reviews dataset [42] for binary text classification. We first show multiscale FNA achieves optimal performance with fewer parameters, indicating a more expressive and powerful mechanism. Adopting a graph-theoretic view of attention interactions, we then perform an ablation study via random edge removal to confirm the superior expressivity of multiscale attention. Finally, using graph spectral analysis and diffusion maps, we elucidate how multiscale attention achieves enhanced expressivity with fewer parameters.

Fewer parameters.

Multiscale attention requires substantially fewer parameters to achieve superior performance. To demonstrate this, we perform a hyperparameter sweep over embedding dimensions d and depths L for all models under Assumption 1 (orthogonality). Because results are robust across all $\alpha < 2$ (see Fig. 5a), we present multiscale attention with $\alpha = 1.2$ as a representative case. In contrast to local attention and DP, multiscale FNA exhibits near-constant performance at all dimensions d

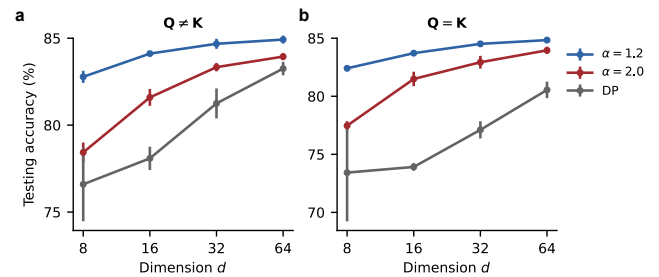


Fig. 3. Effects of embedding dimension and depth. **a** Accuracy on the testing dataset across embedding dimensions d and depth $L = 1$ with $\mathbf{Q} \neq \mathbf{K}$. Dots and error bars show the mean and standard deviation across five trials. **b** Same as **a**, using $\mathbf{Q} = \mathbf{K}$.

and depth $L = 1$ (Fig. 3). This is true even if weight-tying is imposed, significantly reducing the number of parameters (Fig. 3b). Notably, while local attention and DP require multiple layers for their performances to saturate, multiscale FNA achieves the best performance among the three models with just a single layer. In fact, a single-layer multiscale model with one head and $d = 8$, despite its small parameter budget, outperforms a full-size Transformer model with 6 DP layers with 8 attention heads and $d = 512$; we show all full-size results in the following section (Fig. 6). These results indicate that multiscale FNA delivers greater expressivity with far fewer parameters. Practically, this can alleviate the computational bottleneck associated with the complexity of self-attention (i.e., $O(n^2d + d^2n)$ for each attention layer) by enabling lower dimensionality d and fewer layers L , complementing conventional methods that target scaling in n [10, 11, 43].

Greater expressivity.

To demonstrate that FNA’s superior performance, especially in the multiscale regime, arises from a more expressive attention mechanism, we perform an ablation study that progressively suppresses expressivity by randomly masking attention between token pairs with Bernoulli probability p . Viewing the attention mechanism as a graph whose nodes represent tokens and directed edges represent attention, this corresponds to removing a random fraction p of edges. As expected, edge-removal on the pretrained networks with weight-tying leads to decaying accuracies on the testing dataset (Fig. 4). However, across all dimensions d , DP models degrade far less than FNA models: their accuracies remain well above chance level even at $p = 1$, where self-attention is completely absent and only fully-connected layers determine the output. This striking result implies that DP models derive most of their expressivity from the fully-connected layers rather than the attention layers. In contrast, the attention mechanism of FNA models is intrinsic to its expressivity: without it, performance collapses to chance-level. We observe qualitatively similar trends in models without weight-tying, although less pronounced (see Fig. A3 in Appendix A5).

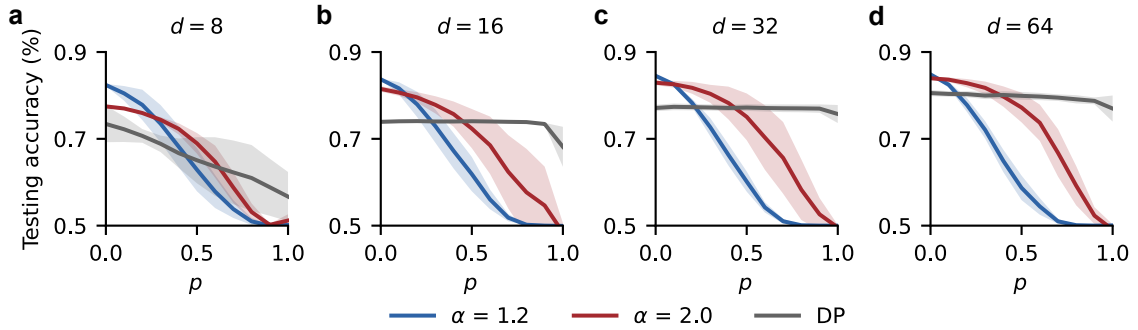


Fig. 4. Ablation of nodes in the attention graph. Accuracy on the testing dataset after randomly ablating nodes from the attention graph with probability p . Lines show the mean across five trials for each network with $\mathbf{Q} = \mathbf{K}$. Shaded regions indicate the standard deviation. **a** $d = 8$. **b** $d = 16$. **c** $d = 32$. **d** $d = 64$.

Mechanistic explanation.

We analyze FNA through the lens of an attention graph: self-attention induces a random-walk process on a directed graph whose nodes are tokens and edges encode attentional interactions. We take the edge weights to be equal to the reciprocal of attention weights, consistent with the intuition that strongly attending tokens are “closer” together. The dynamics of the random walk are governed by spectral properties of the attention matrix \mathbf{A} . In particular, a larger spectral gap $1 - \lambda_2$, where λ_2 is the second eigenvalue of the attention matrix \mathbf{A} , suggests a smaller mixing time—information can flow between nodes (tokens) more rapidly. To test this prediction, we calculate the mean spectral gap across a 10^2 training subset (Fig. 5a). We observe a strong correlation between the spectral gap and testing accuracy for both multiscale FNA and local attention, whereas this relationship is absent for DP; differences among various $\alpha < 2$ are negligible, due to the robustness of multiscale attention explained above. Prior work has also applied the link between spectral gap and mixing time, although through a heuristic argument, to motivate their sparse attention formulation [10]. In contrast, our results reveal that FNA, unlike vanilla attention, admits a predictive index for quantifying performance—the spectral gap—due to its interpretable diffusion formulation.

To further understand the connectivity of tokens within the graph representation, we perform a dimensionality reduction of the token embeddings \mathbf{x} using a diffusion map $\Psi_\tau : \mathbb{R}^n \rightarrow \mathbb{R}^m$:

$$\Psi_\tau(\mathbf{x}) = (\lambda_1^\tau \psi_1(\mathbf{x}), \lambda_2^\tau \psi_2(\mathbf{x}), \dots, \lambda_m^\tau \psi_m(\mathbf{x})), \quad (19)$$

where τ denotes the diffusion time parameter for analyzing pre-trained FNA models. Assuming a connected attention graph based on equation 13, the i -th eigenvalue-eigenvector pair (λ_i, ψ_i) is obtained from the eigendecomposition of the attention weights ordered based on $1 = \lambda_0 \geq \lambda_1 \geq \lambda_2 \geq \dots \geq \lambda_{n-1} > 0$:

$$A_{ij}^\tau(\mathbf{x}) = \sum_{i \geq 0} \lambda_i^\tau \psi_i(\mathbf{x}) \phi_i(\mathbf{x}). \quad (20)$$

The degree of dimensionality reduction based on m is determined by the user based on their own criteria [18]. The

Euclidean distance between the resulting lower-dimensional vectors $\|\Psi_\tau(\mathbf{x}_i) - \Psi_\tau(\mathbf{x}_j)\|$ approximates the diffusion distance $D_t(\mathbf{x}_i, \mathbf{x}_j)$ in equation 36, “Methods”. This measures the similarity between the data points based on their connectivity within a graph structure. It quantifies how easily one can transition from one data point to another assuming a “random walk” process on the graph. Here, the process is differentiated by α with Lévy process ($\alpha < 2$) and Brownian motion ($\alpha = 2$). The time parameter t determines the scale of the structure being considered. Points in proximity with respect to the diffusion distance are more likely to be connected by paths of a certain length, reflecting better information flow from one token to another; the larger the distance, the more restricted is this flow. Applying the diffusion map algorithm with $m = 2$ to the token embeddings of a randomly selected sequence with $n = 500$, we find that the lower-dimensional representations $\Psi_\tau(\mathbf{x})$ are in close proximity for $\alpha = 1.2$ but apart for $\alpha = 2$ (Fig. 5b). Thus, the non-local kernel facilitates long-range interactions between faraway embedding vectors that are otherwise disconnected from the attention graph under the local kernel. We emphasize that the formulation of FNA based on diffusion interactions on a manifold is what enables this interpretable geometric description of the attention weights (see “Methods” for further details).

We further show that this enhanced connectivity of multiscale FNA manifests as shorter path lengths on the attention graph. Intuitively speaking, the shortest path length between token \mathbf{x}_i and token \mathbf{x}_j approximates the number of attention applications required for \mathbf{x}_i to effectively attend to \mathbf{x}_j . Thus, the shortest path length is a meaningful indication of the number of layers needed to realize the full expressivity of an attention mechanism. As an illustrative example, derived from the same 500-length sequence in Fig. 5b, we observe that the words “much” and “danger”—which are adjacent and thus semantically related—are connected by a direct path under $\alpha = 1.2$, but requires shortest paths of length 2 and 13 for $\alpha = 2$ and DP, respectively (Fig. 5c). The matrix of shortest path lengths between any two tokens reveals that this is general across the entire sequence (Fig. 5d): the maximum shortest path lengths are 2, 6 and 14 for $\alpha = 1.2$, $\alpha = 2$ and DP, respectively. By repeating this analysis, we determine

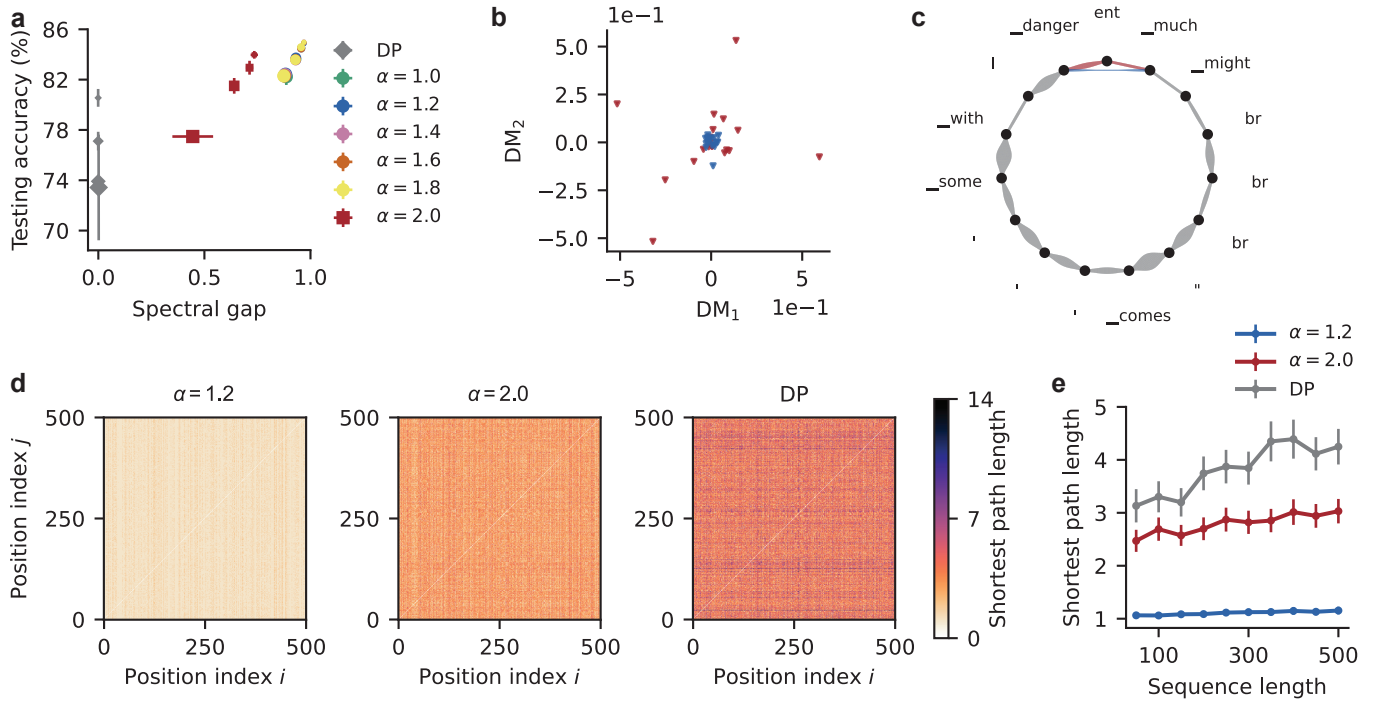


Fig. 5. Graph-theoretic analysis of fractional neural attention. **a** Mean test accuracy across five trials versus the mean spectral gap computed on a random IMDb subset of size 100. Error bars show the standard deviation. **b** Diffusion map visualization with $m = 2$. **c** Attention between two related tokens: “much” and “danger”. The shortest paths for DP, $\alpha = 2$ and $\alpha = 1.2$ are 13, 2 and 1, respectively. Edge widths are proportional to the reciprocal of the attention weight. **d** Shortest-path lengths between every pair of tokens in the same sequence for multiscale FNA ($\alpha = 1.2$), local attention ($\alpha = 2.0$) and DP. **e** Dots show the mean shortest path length between each pair of token in a random sequence of the specific length. Error bars represent 0.2 standard deviations (scaled for clarity).

that these differences in shortest path lengths is robust across all sequence lengths (Fig. 5d). On average, multiscale attention ($\alpha < 2$) requires only one iteration for any token in the sequence to maximally attend to any other, essentially independent of sequence length. In contrast, local attention and DP require additional iterations, growing substantially with sequence length. These results indicate that FNA is particularly effective for long sequences and explain why multiscale attention can achieve optimal performance with only a single layer and small embedding dimensions, while local attention and DP typically need large embedding dimensions or multiple layers for performance to saturate (Fig. 3).

EXPERIMENTS

We evaluate FNA in comparison to standard Transformers across various tasks and modalities, including sentiment analysis and image classification through the architecture of Vision Transformers (ViTs) [6]. We also consider more complex tasks which involve a decoding component such as neural machine translation. Architectures and training details are provided in “Methods”.

Text classification.

We test the model performance on the IMDb dataset using a more realistic model configuration of 6 layers and 8 attention heads. For $\mathbf{W}_{Q,K} \notin O(d)$, FNA model with $\alpha = 1.2$ achieves

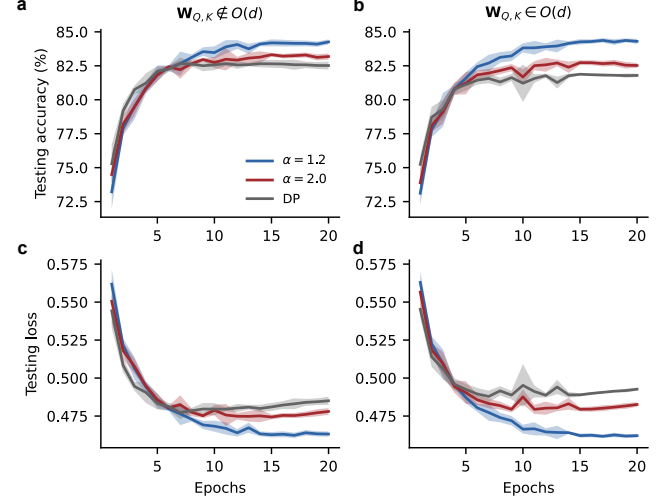


Fig. 6. Learning curves for text classification. **a** Mean test accuracy across five trials for multiscale FNA ($\alpha = 1.2$), local attention ($\alpha = 2.0$) and Transformer (DP) using $\mathbf{W}_{Q,K} \notin O(d)$. The shaded area indicates one standard deviation. **b** Same as a, but with $\mathbf{W}_{Q,K} \in O(d)$. **c** Same as a, but showing test loss. **d** Same as c, but with $\mathbf{W}_{Q,K} \in O(d)$.

the highest median evaluation accuracy by the end of training for 20 epochs across 5 trials (Fig. 6a blue curve). Although

Transformer attains an accuracy of $\sim 81\%$ earlier in the learning process, its performance quickly plateaus after epoch 7, whereas the local attention (red curve) and multiscale FNA (blue curve) models continue to improve (Fig. 6a). When $\mathbf{W}_{Q,K} \in O(d)$, we refer to this as orthogonal projection (op). Under this setting, the overall behavior remains similar; however, the test accuracy gap between op-FNA ($\alpha = 1.2$) and op-DP widens further (Fig. 6b). The loss curves for all models reflect their corresponding accuracies (Fig. 6c,d), showing an overall decreasing trend. However, FNA (blue curves) exhibits the smallest degradation for both cases of $\mathbf{W}_{Q,K} \notin O(d)$ and $\mathbf{W}_{Q,K} \in O(d)$. The overall accuracies of the 6-layer models can already be matched by the single-layer models in Fig. 3, with multiscale FNA exhibiting superior trainability. We summarize the model performances in Table I.

Model	Mean	Median	Best	Worst
FNA	84.14%	84.26%	84.33%	83.88%
LA	83.10%	83.18%	83.42%	82.80%
DP	82.57%	82.52%	82.00%	82.25%
op-FNA	84.25%	84.30%	84.44%	83.97%
op-LA	82.56%	82.52%	82.81%	82.29%
op-DP	81.79%	81.79%	81.99%	81.63%

TABLE I. Test accuracy on IMDb dataset acquired over 5 independent iterations. Best performance of each category is bold while the second best is underlined.

Image processing.

Following standard practice, we treat an image as a sequence by feeding ordered, fixed-size patches into the attention mechanism, yielding a ViT architecture [6]. We train FNA-based models and compare them with a Transformer baseline on CIFAR-10 [44], and also examine the effect of enforcing Assumption 1 (orthogonality).

At the end of training, multiscale FNA ($\alpha = 1.2$) achieves a mean accuracy of 76.17%, surpassing its local counterpart (75.14%) and slightly outperforming the Transformer baseline (76.03%) (Fig. 7a). When orthogonality is enforced ($\mathbf{W}_{Q,K} \in O(d)$), multiscale FNA exhibits a minor performance drop yet still exceeds the Transformer, whose mean accuracy remains nearly unchanged at 76.07%. In contrast, both LA and DP show more noticeable degradation, reaching 75.73% and 75.25%, respectively (Fig. 7b). Opposite trends are observed for the test loss in Fig. 7c–d.

Machine translation.

Having established FNA’s advantages on text and image classification, we next evaluate it on a translation task that introduces a decoder in addition to the encoder, making the problem substantially more challenging. We train all models on the Multi30K English–German (En-De) dataset [20], using 30 training epochs and 5 independent runs per configuration. Multiscale FNA achieves higher BLEU (bilingual evaluation understudy) scores [45] than both local attention and DP; summary results are reported in Table 2, with training curves in Fig. A4 (see Appendix A 6).

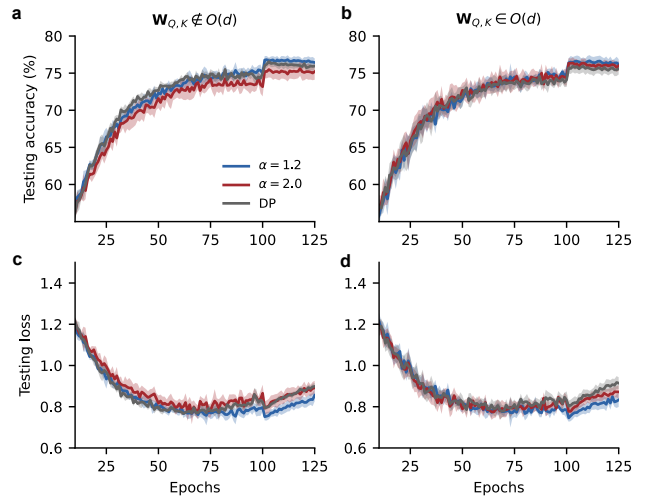


Fig. 7. CIFAR10 classification. **a** Mean test accuracy percentage for 4-layer and 6-attention-head FNA, local attention and Transformer (DP) over 5 trials for $\mathbf{W}_{Q,K} \notin O(d)$. The lower and upper parts of the color shade represent the standard deviation over the 5 trials at each epoch. The blue and red curves represent multiscale FNA ($\alpha = 1.2$) and local attention ($\alpha = 2$), respectively. **b** Same as **a**, but with $\mathbf{W}_{Q,K} \in O(d)$. **c** Same as **a**, but showing test loss. **d** Same as **c**, but with $\mathbf{W}_{Q,K} \in O(d)$.

Model	$\mathbf{W}_{Q,K} \notin O(d)$	$\mathbf{W}_{Q,K} \in O(d)$
FNA	34.64 \pm 0.37	33.54 \pm 0.38
LA	34.13 ± 0.46	32.85 ± 0.36
DP	34.00 ± 0.68	33.19 ± 0.68

TABLE II. The mean BLEU score and its standard deviation across 5 iterations for each model.

DISCUSSION

In this study, we have introduced fractional neural attention (FNA), a novel neuroscience-inspired attention framework that unifies principles of attentional sampling with dynamical systems, network theory, and Transformer architectures. FNA naturally captures token interactions across multiple scales, yielding greater expressivity and faster information mixing, and thus advances the foundational capacity of Transformers. Theoretically, we have illustrated that the dynamics of FNA are governed by a partial differential equation mechanistically linked to the fractional Laplacian, and that larger spectral gaps and shorter path lengths in the induced attention networks underlie its computational advantages. Empirically, FNA matches or exceeds Transformer baselines across text, vision, and machine translation tasks, indicating substantial headroom for scaling to larger models.

A growing line of work has approached attention mechanisms through the lenses of stochastic and dynamical systems, treating token embeddings as spatial variables and depth as a time component [8, 23–25]. For instance, the transformation of token embeddings in a sequence as they pass through Transformer layers has been interpreted as the evolution of a multi-particle system using numerical methods like the Lie-

Trotter splitting scheme [8]. Bridging deep neural networks with ODEs [27] has also been adopted in other studies to understand and describe the geometry of learned representations of Transformers with time-independent weights [25]. In a similar vein, this framework enables the application of measure-theoretic tools to investigate the regularity properties of Transformers [23, 24]. Additionally, under suitable normalization—e.g., through the Sinkhorn algorithm to enforce bistochasticity on attention scores and additional conditions on the projection matrices—the resulting push-forward map converges to a local Laplace operator, yielding heat-equation dynamics (Brownian motion) for self-attention [9]. In contrast, Fractional Neural Attention (FNA) yields an operator-level non-local limit governed by the fractional Laplacian, linking attention directly to α -stable Lévy dynamics with multiscale, power-law interactions rather than Brownian diffusion [17].

FNA enables multiscale coupling of short- and long-range interactions simultaneously, because its update rule is driven by a fractional operator. This differs fundamentally from engineered local-global hybrids that hard-code two scales. For instance, Longformer combines sliding-window attention with a small set of global tokens to capture local and document-level dependencies [11]; BigBird introduces block-sparse patterns with global, random, and local links to ensure theoretical completeness and scalability [10]; and Nyströmformer approximates full attention with landmark-based low-rank kernels [46]. These designs reliably extend reach and improve efficiency, but their local-global behavior arises from hand-crafted patterns (such as window sizes, dilation rates, landmark choices) rather than from a single governing operator. In FNA, fractional diffusion is built into the attention rule, yielding a principled mechanism for multiscale coupling. A single parameter α determines the heaviness of the interaction tail. For $\alpha < 2$, the operator induces scale-free, power-law coupling across all distances, causing multiscale behavior to emerge intrinsically rather than through manually designed connectivity. When $\alpha = 2$, the operator reduces to the local attention case, which coincides exactly with a previous attention formulation that ensures Lipschitz continuity [35]. This also suggests that the multiscale FNA map retains regularity properties, which can stabilize training [47] and facilitate the construction of flow-based generative models [48, 49].

Related “non-local” neural networks introduce global dependencies by summing over all positions with learned weights [50]. In contrast, FNA’s non-locality arises from the fractional Laplacian: it modifies the law of interaction (the kernel that governs how influence decays with distance), not merely the connectivity pattern, yielding a unified and interpretable geometric–stochastic foundation. Analyzing FNA through an attention-network perspective reveals that self-attention defines a discrete random walk analogous to a Lévy process whose mixing speed is governed by the spectral gap of the attention matrix. Empirically, FNA exhibits a strong correlation between model performance and spectral gap, indicating faster information mixing while maintaining robustness across different fractional orders $\alpha < 2$. This connection between mixing speed and model efficiency parallels the motivation behind BigBird [10], where sparse attention patterns approximate Erdős–Rényi

graphs with large spectral gaps and rapid mixing. By contrast, FNA achieves efficiency without imposing sparsity-inducing inductive biases: it delivers substantial parameter reductions (fewer layers and lower embedding dimensions) while concentrating a greater portion of information processing within the attention mechanism itself, thereby aligning the model architecture more closely with the data geometry than the original Transformer.

It is important to note that natural data, from images [51–53] to language sequences [54], often exhibit fractal structure, nested multiscales and heavy-tailed statistics. FNA aligns with these statistics by introducing self-similar, power-law interactions characteristic of Lévy processes, enabling efficient information mixing. More broadly, nested multiscale organization is central to diverse cognitive functions [55–57]; FNA thus offers a unifying principle linking biological and artificial intelligence, and could catalyze deeper, synergistic interactions between neuroscience and modern AI [14, 15].

METHODS

Riemannian manifold

Throughout this paper, we only consider Riemannian manifolds \mathcal{M} . Provided the local coordinates, its volume form is $d\text{vol}_{\mathbf{x}} := \sqrt{|g|} dx^1 \wedge \cdots \wedge dx^n$ where $|g|$ is the absolute value of the determinant of the matrix representation of the metric tensor on \mathcal{M} . Additionally, we use $d_g : \mathcal{M} \times \mathcal{M} \rightarrow \mathbb{R}^+$ to represent the geodesic metric. That is, for $\mathbf{x}, \mathbf{y} \in \mathcal{M}$,

$$d_g(\mathbf{x}, \mathbf{y}) = \inf_{\gamma} \int_0^1 \sqrt{g_{\gamma(t)}(\nabla \gamma(t), \nabla \gamma(t))} dt. \quad (21)$$

is the infimum over piecewise differentiable paths $\gamma : [0, 1] \rightarrow \mathcal{M}$ between $\gamma(0) = \mathbf{x}$ and $\gamma(1) = \mathbf{y}$.

Fractional Laplacian on manifolds

Given a closed and compact manifold \mathcal{M} as well as a square integrable function $u \in L^2(\mathcal{M})$, the fractional Laplacian is defined spectrally through

$$(-\Delta_{\mathcal{M}})^{\alpha/2} u(\mathbf{x}) := \sum_{i=1}^{\infty} \lambda_i^{\alpha/2} \langle u, \phi_i \rangle_{L^2(\mathcal{M})} \phi_i(\mathbf{x}) \quad (22)$$

for \mathbf{x} in the fractional Laplacian domain. Given the compactness of the manifold, the set $\{\phi_i\}_{i=1}^{\infty}$ composes the orthonormal eigenfunctions through $-\Delta_{\mathcal{M}} \phi_i = \lambda_i \phi_i$ with countably many eigenvalues that satisfy $0 = \lambda_1 < \lambda_2 \leq \lambda_3 \leq \cdots$ with $\lim_{i \rightarrow \infty} \lambda_i = \infty$.

Heat kernel

A function $k : [0, \infty) \times \mathcal{M} \times \mathcal{M} \rightarrow [0, \infty)$ is a heat kernel if for almost every $\mathbf{x}, \mathbf{y} \in \mathcal{M}$ and $\forall s, t \geq 0$:

1. Positivity: $k_t(\mathbf{x}, \mathbf{y}) \geq 0$.
2. Total mass inequality: $\int_{\mathbf{y} \in \mathcal{M}} k_t(\mathbf{x}, \mathbf{y}) d\text{vol}_{\mathbf{y}} \leq 1$.
3. Symmetry: $k_t(\mathbf{x}, \mathbf{y}) = k_t(\mathbf{y}, \mathbf{x})$.
4. Semi-group: $k_{s+t}(\mathbf{x}, \mathbf{y}) = \int_{\mathbf{z} \in \mathcal{M}} k_s(\mathbf{x}, \mathbf{z}) k_t(\mathbf{z}, \mathbf{y}) d\text{vol}_{\mathbf{z}}$.

5. Approximation of identity:

$$\lim_{t \rightarrow 0^+} \left\| \int_{y \in \mathcal{M}} k_t(\mathbf{x}, \mathbf{y}) f(\mathbf{y}) d\text{vol}_y - f(\mathbf{x}) \right\|_{L^2(\mathcal{M}, g)} = 0, \quad (23)$$

for $f \in L^2(\mathcal{M}, g)$.

Every heat kernel gives rise to an associated semigroup

$$\mathcal{K}_t f(\mathbf{x}) = \int_{y \in \mathcal{M}} k_t(\mathbf{x}, \mathbf{y}) f(\mathbf{y}) d\text{vol}_y. \quad (24)$$

A semigroup also gives rise to a quadratic form

$$\xi(f) = \lim_{t \rightarrow 0^+} \left\langle \frac{f - \mathcal{K}_t f}{t}, f \right\rangle_{L^2(\mathcal{M}, g)}. \quad (25)$$

We define $d_g : \mathcal{M} \times \mathcal{M} \rightarrow \mathbb{R}^+$ as the geodesic metric given g , which is the determinant of the matrix representation of the metric tensor on \mathcal{M} . In general, heat kernels can take various forms, but must satisfy the conditions outlined above. Our focus will be on stochastically complete heat kernels, which means they are normalized, or equivalently, the corresponding semigroups satisfy $\mathcal{K}_t 1 = 1 \forall t > 0$ (equation (24)).

A quadratic form is regular if there exists a set C of continuous functions with compact support ($C_c(\mathcal{M})$) that are also in the domain $\mathcal{D}(\xi)$ of ξ , i.e., $C \subset C_c(\mathcal{M}) \cap \mathcal{D}(\xi)$ such that C is dense both in $C_c(\mathcal{M})$ and $\mathcal{D}(\xi)$ under appropriate norms [19]. The heat kernel dichotomy [32] holds under two conditions:

1. All balls defined with metric d_g in \mathcal{M} are relatively compact;
2. The heat kernel $k_t(\mathbf{x}, \mathbf{y})$ is a stochastically complete and α -scale invariant heat kernel such that the associated quadratic form is regular.

Lévy process

A Lévy α -stable distribution (often termed stable distribution) [58], is defined by a characteristic function involving a tuple $(\alpha, \beta, \sigma, \mu)$ containing the stable, skewness, scale and location parameters respectively,

$$\varphi(u; \alpha, \beta, \sigma, \mu) = e^{-|\sigma u|^\alpha (1 - i\beta \text{sgn}(u) \zeta(u; \alpha)) + iu\mu} \quad (26)$$

where $\text{sgn}(u)$ is the sign of u and

$$\zeta(u; \alpha) = \begin{cases} \tan\left(\frac{\pi\alpha}{2}\right) & \alpha \neq 1 \\ -\frac{2}{\pi} \log|u| & \alpha = 1 \end{cases}.$$

Let us consider a random variable X drawn from a stable distribution, i.e., $X \sim S_\alpha(\beta, \sigma, \mu)$. If it is symmetric and centered with $\beta = \mu = 0$ (i.e., $X \sim S_\alpha(\sigma)$), it is referred to as $S\alpha S$ (symmetric α stable) [59]. For $\alpha < 2$, the random variable associated with the stable distribution has infinite m^{th} -moment for $m \geq \alpha$.

A $(S\alpha S)$ Lévy process L_t is a stochastic process with:

1. $L_0 = 0$.
2. L_t has independent increments.

3. $(L_t - L_s) \sim S_\alpha((t - s)^{1/\alpha})$ for all $0 \leq s \leq t$.

4. L_t is stochastically continuous.

5. L_t is RCLL (right continuous with left limits) almost surely.

Orthogonal projection for single-head attention

We now present the proof for Proposition 1.

Proof. In \mathbb{R}^d , the distance between each query-key pair under Assumption 1 follows

$$\begin{aligned} \|\mathbf{Q}_i - \mathbf{K}_j\| &= (\|\mathbf{Q}_i\|^2 - 2\mathbf{Q}_i^\top \mathbf{K}_j + \|\mathbf{K}_j\|^2)^{1/2}, \\ &= (\|\mathbf{W}_Q \mathbf{x}_i\|^2 - 2\mathbf{x}_i^\top \mathbf{W}_Q^\top \mathbf{W}_K \mathbf{x}_j + \|\mathbf{W}_K \mathbf{x}_j\|^2)^{1/2}, \\ &= (\|\mathbf{x}_i\|^2 - 2\mathbf{x}_i^\top \tilde{\mathbf{W}}_K \mathbf{x}_j + \|\mathbf{x}_j\|^2)^{1/2}, \\ &= \|\mathbf{x}_i - \tilde{\mathbf{W}}_K \mathbf{x}_j\|, \\ &= \|\tilde{\mathbf{Q}}_i - \tilde{\mathbf{K}}_j\|, \end{aligned}$$

where $\tilde{\mathbf{W}}_K := \mathbf{W}_Q^\top \mathbf{W}_K \in O(d)$, allowing us to set without loss of generality $\mathbf{Q} = \mathbf{x}$ and $\mathbf{K} := \tilde{\mathbf{W}}_K \mathbf{x}$. For $\mathcal{M} = \mathbb{S}^{d-1}$, the geodesic is simply the great circle $d_g(\mathbf{Q}_i, \mathbf{K}_j) = \cos^{-1}(\mathbf{Q}_i^\top \mathbf{K}_j)$. Following a similar line of reasoning, this result naturally extends to the spherical manifold. \square

Based on the result of Proposition 1, for architectures satisfying Assumption 1 (orthogonality) in the main text, we implement the following configurations:

- When $\mathbf{Q} \neq \mathbf{K}$, we set $\mathbf{W}_Q = \mathbf{I}$, $\mathbf{W}_K \in O(d)$.
- When $\mathbf{Q} = \mathbf{K}$, we set $\mathbf{W}_Q = \mathbf{W}_K = \mathbf{I}$.

When the numbers of attention heads $H > 1$, for each attention head, the corresponding submatrix of $\mathbf{W}_{Q,K}$ is instead semi-orthogonal and no longer qualifies as an isometry, i.e., $d_g(\mathbf{q}_i, \mathbf{k}_j) = d_g(\mathbf{x}_i, \mathbf{x}_j)$. See Appendix A 3 for a detailed discussion.

Convergence of PDEs

We prove Theorem 2 by first showing the following lemma.

Lemma 1. *The infinitesimal generator from the normalization scheme in the main text yields*

$$\mathcal{H}f = -c \frac{(-\Delta)^{\alpha/2}(f\rho) - f(-\Delta)^{\alpha/2}\rho}{\rho}. \quad (27)$$

Proof. Step 1: Similar to the standard case, we start from the diffusion equation [18, 60]

$$u_t = -c(-\Delta)^{\alpha/2}u, \quad u(\mathbf{x}, 0) = g(\mathbf{x}) \quad (28)$$

for $\mathbf{x} \in \mathcal{M}$. The solution at time $t = \varepsilon$ is

$$u(\mathbf{x}, \varepsilon) = \frac{1}{Z_{\alpha, d}} \int_{\mathcal{M}} k_\varepsilon(\mathbf{x}, \mathbf{x}') g(\mathbf{x}') d\text{vol}_{\mathbf{x}'} \quad (29)$$

where $Z_{\alpha,d}$ is the normalization constant and k_ε depends on α . For small ε , we can approximate $u(\mathbf{x}, \varepsilon)$ through a Taylor expansion

$$\begin{aligned} u(\mathbf{x}, \varepsilon) &= u(\mathbf{x}, 0) + \frac{\partial}{\partial t} u(\mathbf{x}, 0) \varepsilon + O(\varepsilon^2) \\ &= g - \varepsilon c(-\Delta)^{\alpha/2} g + O(\varepsilon^2). \end{aligned} \quad (30)$$

Step 2: The row normalization scheme is applied to the FNA score (equation 13) via

$$\text{FAttn}[f](\mathbf{q}) := \frac{\sum_j \Phi_\alpha\left(\frac{d_g(\mathbf{q}, \mathbf{k}_j)}{\varepsilon^{1/\alpha}}\right) f(\mathbf{k}_j)}{\sum_j \Phi_\alpha\left(\frac{d_g(\mathbf{q}, \mathbf{k}_j)}{\varepsilon^{1/\alpha}}\right)} = \frac{\frac{1}{n} \sum_j \Phi_\alpha\left(\frac{d_g(\mathbf{x}, \mathbf{x}_j)}{\varepsilon^{1/\alpha}}\right) f(\mathbf{x}_j)}{\frac{1}{n} \sum_j \Phi_\alpha\left(\frac{d_g(\mathbf{x}, \mathbf{x}_j)}{\varepsilon^{1/\alpha}}\right)}, \quad (31)$$

where the second equality is established under the condition of Assumption 1 & 2, resulting in $d_g(\mathbf{q}_i, \mathbf{k}_i) = d_g(\mathbf{W}_Q \mathbf{x}_i, \mathbf{W}_K \mathbf{x}_j) = d_g(\mathbf{x}_i, \mathbf{x}_j)$ (i.e., isometry).

Step 3: After taking the limit $n \rightarrow \infty$, obtain the expression for the Taylor expansion w.r.t ε :

$$\begin{aligned} \lim_{n \rightarrow \infty} \frac{\frac{1}{n} \sum_j \Phi\left(\frac{d_g(\mathbf{x}, \mathbf{x}_j)}{\varepsilon^{1/\alpha}}\right) f(\mathbf{x}_j)}{\frac{1}{n} \sum_j \Phi\left(\frac{d_g(\mathbf{x}, \mathbf{x}_j)}{\varepsilon^{1/\alpha}}\right)} &= \frac{\int_{\mathcal{M}} k_\varepsilon(\mathbf{x}, \mathbf{x}') f(\mathbf{x}') \rho(\mathbf{x}') d\text{vol}_{\mathbf{x}'}}{\int_{\mathcal{M}} k_\varepsilon(\mathbf{x}, \mathbf{x}') \rho(\mathbf{x}') d\text{vol}_{\mathbf{x}'}} = T_{\mu,t}^{\text{FNA}}[f](\mathbf{x}) \\ &= \frac{(f\rho)(\mathbf{x}) - \varepsilon c(-\Delta)^{\alpha/2} (f\rho)(\mathbf{x}) + O(\varepsilon^2)}{\rho(\mathbf{x}) - \varepsilon c(-\Delta)^{\alpha/2} \rho(\mathbf{x}) + O(\varepsilon^2)} \\ &\stackrel{(\star)}{=} \left[(f\rho)(\mathbf{x}) - \varepsilon c(-\Delta)^{\alpha/2} (f\rho)(\mathbf{x}) + O(\varepsilon^2) \right] \frac{1}{\rho(\mathbf{x})} \left(1 + \varepsilon \frac{(-\Delta)^{\alpha/2} \rho(\mathbf{x})}{\rho(\mathbf{x})} + O(\varepsilon^2) \right) \\ &= f(\mathbf{x}) - \frac{\varepsilon c(-\Delta)^{\alpha/2} (f\rho)(\mathbf{x})}{\rho(\mathbf{x})} + \varepsilon c f(\mathbf{x}) \frac{(-\Delta)^{\alpha/2} \rho(\mathbf{x})}{\rho(\mathbf{x})} + O(\varepsilon^2) \\ &= f(\mathbf{x}) - \varepsilon \frac{c}{\rho(\mathbf{x})} \left((-\Delta)^{\alpha/2} (f\rho)(\mathbf{x}) - f(\mathbf{x}) (-\Delta)^{\alpha/2} (\rho)(\mathbf{x}) \right) + O(\varepsilon^2). \end{aligned}$$

The third equality (\star) is obtained through the expansion of the function $h(z) = 1/z$ applied to:

$$\frac{1}{\rho - \varepsilon c(-\Delta)^{\alpha/2} \rho + O(\varepsilon^2)} = \frac{1}{\rho} \left(1 + \varepsilon \frac{(-\Delta)^{\alpha/2} \rho}{\rho} + O(\varepsilon^2) \right).$$

We conclude the proof by taking the limit of $\varepsilon \rightarrow 0$

$$\mathcal{H}^{\text{FNA}}[f] := \lim_{\varepsilon \rightarrow 0} \frac{T_{\mu,t}^{\text{FNA}}[f](\mathbf{x}) - f(\mathbf{x})}{\varepsilon}. \quad (32)$$

□

Experiments

Hardware. All model training and pretrained analysis were realized on Tesla V100-SXM2-32GB GPUs.

Text classification. We conducted two sets of model training experiments for text classification as described in the main text: shallow models of depth 1 and 2 (Fig. 3), and deeper 6-layer models (Fig. 6).

In Fig. 3, we focus on single-head attention models ($H = 1$) that satisfy Assumption 1 (orthogonality), and further examine both cases where Assumption 2 (symmetry) holds and where it does not. We perform a parameter sweep over depths $L \in$

1, 2 and embedding dimensions $d \in 8, 16, 32, 64$, with fully connected hidden layers fixed at 256. Each configuration is trained for 25 epochs across 5 independent runs using Adam [61], with an initial learning rate of 1×10^{-4} decayed by a factor of 5 at epoch 19, and a batch size of 16. The FNA models are trained for fractional orders $\alpha \in \{1, 1.2, 1.4, 1.6, 1.8, 2\}$.

In Fig. 6, all models have 6 layers, 8 attention heads, an embedding dimension of 256 and are trained for 20 epochs. We use an initial learning rate of 10^{-4} and decay it by a factor of 10 at epoch 15. The batch size is set to 32.

For both sets of text classification experiments, we set the maximal sequence length to 512 and the momentum terms in Adam to $(\beta_1, \beta_2) = (0.9, 0.999)$. No weight decay is deployed. For all text classification tasks, we use the distance scaling $\kappa = \frac{\sqrt{d_H}}{2^{1/d_H-1}}$ for multiscale FNA ($\alpha < 2$) where $d_H = d/H$ is the head dimension. We also set $d_{\mathcal{M}} = d_H$ in Φ_α (equation 10), consistent with the canonical choice in fractional diffusion maps [19] when $H = 1$. For $\alpha = 2$, we set $\kappa = \sqrt{d_H}$ for this and all other task types. This choice aligns with prior practices using the dot product [1] or (squared) Euclidean distance [35], ensuring that the resulting values do not become excessively large and push the softmax function into regions with vanishing gradients.

Attention graph node ablation. In Figs. 4 and A3, we con-

sider the Bernoulli probability $p = 0, 0.1, 0.2, \dots, 1$, of random node removal by masking its corresponding index location in the attention score (along the column). This experiment is carried out on all pretrained single-layer Transformers in Fig. 3. During inference, the batch size is set to 64.

Markov chain diagonalization. Let us define the diagonal matrix \mathbf{D} defined by $D_{ii} = \sum_j \tilde{C}_{ij}$, then the attention weight matrix $\tilde{\mathbf{A}}$ in equation 14 is adjoint to the symmetrical matrix [39]

$$\hat{\mathbf{A}} := \mathbf{D}^{-1/2} \tilde{\mathbf{C}} \mathbf{D}^{-1/2}. \quad (33)$$

Thus, $\hat{\mathbf{A}}$ shares the same set of eigenvalues as $\tilde{\mathbf{A}}$ which are all real and does not need to be explicitly computed:

$$1 = \eta_0 \geq \eta_2 \geq \dots \geq \eta_{n-1}. \quad (34)$$

If floating point errors cause $\hat{\mathbf{A}}$ to be asymmetrical, the matrix $(\hat{\mathbf{A}} + \hat{\mathbf{A}}^\top)/2$ can be used for diagonalization in its place to guarantee numerical stability. Additionally, the eigenvectors of $\hat{\mathbf{A}}$ form an orthonormal basis $\{\mathbf{v}_j\}_{j=0}^{n-1}$. The left and right eigenvectors of $\tilde{\mathbf{A}}$, denoted ϕ_j and ψ_j are related to \mathbf{v}_j through

$$\phi_j = \mathbf{D}^{1/2} \mathbf{v}_j, \quad \psi_j = \mathbf{D}^{-1/2} \mathbf{v}_j \quad (35)$$

and they are also bi-orthonormal, i.e., $\langle \phi_i, \psi_j \rangle = \delta_{i,j}$.

In Fig. 2a, we use the setting $\mathbf{W}_Q = \mathbf{W}_K = \mathbf{I}$ and single attention head $H = 1$. To compute $\tilde{\mathbf{C}}$, we set $\kappa = \sqrt{\varepsilon}$ in equation 13 with the bandwidth parameter $\varepsilon = 1 \times 10^{-4}$. The eigenvalues of $\tilde{\mathbf{A}}$ are then computed following the same procedure described above to generate the figure. By setting $t = \varepsilon^{\alpha/2}$, the fractional Laplacian eigenvalues $\lambda_i = -t^{-1} \log \eta_i$ and the eigenfunctions ψ_i satisfy $\tilde{\mathbf{A}}\psi_i = e^{t\lambda_i} \psi_i$ for the heat kernel as in equation A5 (see Appendix A4).

Diffusion maps for FNA. Diffusion map analyses are performed under Assumptions 1 and 2 stated in the main text. For sequences with the maximum length $n = n_{\max}$, the entire sequence is retained. For shorter sequences ($n < n_{\max}$), as padding masks are applied to the final $(n_{\max} - n)$ keys but not queries, we truncate all padding indices and operate on the resulting $n \times n$ fractional attention score matrix $\tilde{\mathbf{C}}$ (equation 13) in order to guarantee the symmetry condition $\mathbf{Q} = \mathbf{K}$.

The diffusion map embeddings in Fig. 5b are obtained through the diffusion maps algorithm with the top two components in equation 19. Additionally, we compute the center of the token embeddings and plot only those tokens whose Euclidean distance from the center exceeds 5.95 (units). We compute $\tilde{\mathbf{C}}$ by setting $\kappa = \frac{\sqrt{d_H}}{2^{1/d_H} - 1} \sqrt{\varepsilon}$ where $\varepsilon = 0.1$. The diagonalization method for the fractional self-attention weights (equation 14) is detailed above. This allows us to establish the eigen-decomposition (equation 20) where ϕ_i and ψ_i are the left and right eigenvectors of $\tilde{\mathbf{A}}$; λ_i are the corresponding eigenvalues. The diffusion distance between two points is defined by

$$\begin{aligned} D_\tau^2(\mathbf{x}_i, \mathbf{x}_j) &= \left\| p(\tau, \mathbf{y} | \mathbf{x}_i) - p(\tau, \mathbf{y} | \mathbf{x}_j) \right\|_w^2 \\ &= \sum_{\mathbf{y}} \left(p(\tau, \mathbf{y} | \mathbf{x}_i) - p(\tau, \mathbf{y} | \mathbf{x}_j) \right)^2 w(\mathbf{y}) \end{aligned} \quad (36)$$

with the weight function $w(\mathbf{y}) = 1/\phi_0(\mathbf{y})$ accounting for the (empirical) local density of points [18, 39]. The following result establishes the diffusion distance and the Euclidean distance in the diffusion map space with all $n - 1$ eigenvectors:

$$D_\tau^2(\mathbf{x}_i, \mathbf{x}_j) = \left\| \Psi_\tau(\mathbf{x}_i) - \Psi_\tau(\mathbf{x}_j) \right\|^2. \quad (37)$$

Visual processing. In Fig. 7, the models with 4 layers and 6 attention heads are trained for 125 epochs. We use Adam with an initial learning rate of 5×10^{-4} and decay it by a factor of 10 at epoch 100. Batch size is set to 64. The momentum terms are set as $(\beta_1, \beta_2) = (0.9, 0.95)$. No weight decay is deployed. We set $\kappa = d_H$ in equation 13.

Translation. We use the same architecture setting as in [1]. Each model contains 6 encoding and decoding layers with 8 attention heads. We set $\kappa = d_H$ in equation 13. We use Adam with an initial learning rate of 2.2×10^{-4} for $\mathbf{W}_{Q,K} \in O(d)$ (orthogonal), and 2×10^{-4} for the (general) case $\mathbf{W}_{Q,K} \notin O(d)$. We employ PyTorch’s ReduceLROnPlateau learning scheme with a reduction factor of 0.75. The learning rate schedule is shown in Fig. A5 in Appendix A6. The momentum terms are set as $(\beta_1, \beta_2) = (0.9, 0.98)$; no weight decay is deployed.

Data availability All data from this study will be made available in a Zenodo repository.

Code availability The code used for the simulations and analyses of the FNA models and Transformer training will be made available upon submission.

Appendix A

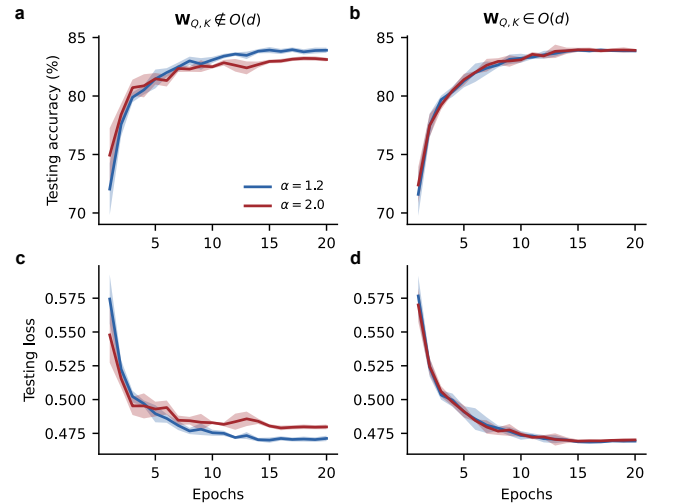


Fig. A1. Learning curves for text classification. **a** Mean test accuracy across five trials for multiscale FNA ($\alpha = 1.2$) and local attention ($\alpha = 2$) using $\mathbf{W}_{Q,K} \notin O(d)$. The shaded area indicates one standard deviation. **b** Same as **a**, but with $\mathbf{W}_{Q,K} \in O(d)$. **c** Same as **a**, but showing test loss. **d** Same as **c**, but with $\mathbf{W}_{Q,K} \in O(d)$.

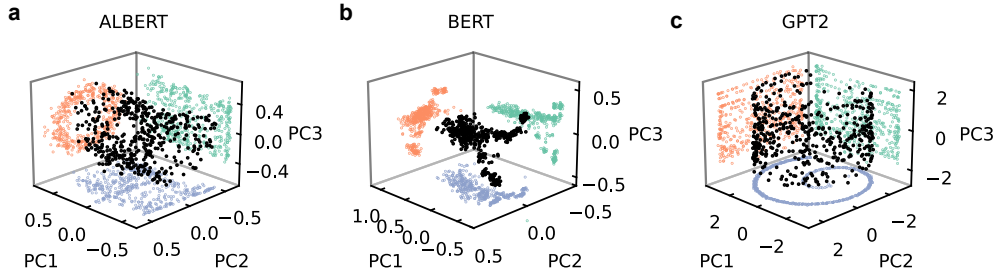


Fig. A2. PCA of token embeddings. (a–c) Top 3 principal components of embeddings of a random input sentence (generated by GPT2) represented by scattered black dots for pretrained ALBERT, BERT and GPT2 respectively. The other colored points are the projections onto two principal components, i.e., blue for PC1 vs PC2, green for PC1 and PC3 and orange for PC2 and PC3.

1. FNA on spherical manifold

By applying an explicit L^2 -normalization to the embeddings \mathbf{X} , one can naturally project them onto the unit sphere \mathbb{S}^{d-1} . In this spherical setting, the Euclidean distance $\|\mathbf{q}_i - \mathbf{k}_j\|$ in equation 13 is replaced by the geodesic distance on the sphere:

$$d_g(\mathbf{q}_i, \mathbf{k}_j) := d_g(\iota_Q(\mathbf{x}_i), \iota_K(\mathbf{x}_j)) = \arccos(\mathbf{x}_i^\top \mathbf{W}_Q^\top \mathbf{W}_K \mathbf{x}_j).$$

Note that the isometric embedding will generally not hold if $\mathbf{W}_{Q,K} \notin O(d)$. In order to guarantee the well-posedness of $d_g(\mathbf{q}_i, \mathbf{k}_j)$, we define

$$\iota_{Q,K}(\mathbf{x}) = \begin{cases} \mathbf{W}_{Q,K} \mathbf{x} & \text{if } \mathbf{W}_{Q,K} \in O(d) \\ \frac{\mathbf{W}_{Q,K} \mathbf{x}}{\|\mathbf{W}_{Q,K} \mathbf{x}\|} & \text{otherwise.} \end{cases} \quad (\text{A1})$$

Now, the FNA score as in equation 13 for $\alpha < 2$ is instead defined by

$$\tilde{C}_{i,j} := \Phi_\alpha \left(\frac{d_g(\iota_Q(\mathbf{x}_i), \iota_K(\mathbf{x}_j))}{\kappa} \right) \quad (\text{A2})$$

Due to floating point errors, we mask the values of query-key dot products $\iota_Q(\mathbf{x}_i)^\top \iota_K(\mathbf{x}_j)$ that fall below -1 and exceed 1 by -1 and 1 respectively. This bounds the query-key dot-product within $[-1, 1]$, ensuring the domain of arccos function remains well-defined. Similar to the Euclidean case (\mathbb{R}^d), the non-local kernel $\Phi_\alpha(z)$ explicitly depends on d . For multiscale FNA ($\alpha < 2$), we use the scale parameter $\kappa = \frac{\pi}{\pi^{1/d_M} - 1}$. When $H = 1$ (single attention-head), the intrinsic dimension of the manifold satisfies $d_M = d - 1$. Otherwise, we set $d_M = d_H$ in Φ_α (equation 10). For local attention ($\alpha = 2$), we use $\kappa = 1$. Additionally, as the maximum distance between any two points on $r\mathbb{S}^{d-1}$ is πr ($r := \kappa^{-1}$), this acts as the masking value for $d_g(\iota_Q(\mathbf{x}_i), \iota_K(\mathbf{x}_j))$.

Using the same settings as in the main text, we evaluate the spherical variant of FNA on the IMDb dataset. The initial learning rate is set to 1.2×10^{-5} and decayed by a factor of 10 at epoch 15. The corresponding training curves and performance results are shown in Fig. A1 and Table III, respectively.

2. Distribution of token embeddings

To highlight the non-uniformity of ρ in Theorem 2, we examine the embeddings of an identical input sequence in three different, popular, pre-trained Transformer models: ALBERT

Model	Mean	Median	Best	Worst
FNA	83.83%	83.91%	84.06%	83.41%
LA	83.08%	83.12%	83.27%	82.86%
op-FNA	83.86%	83.85%	84.02%	83.75%
op-LA	83.83%	83.90%	83.96%	83.66%

TABLE III. Test accuracy on IMDb dataset acquired over 5 independent iterations. We use the setting $\mathcal{M} := \mathbb{S}^{d-1}$. Best performance of each category is bold.

[62], BERT [63] and GPT2 [64]. In Fig. A2a, c, ALBERT and GPT2 reveal circular and spiral patterns, respectively. These geometrical structures have been linked to the encoding of positional information within a sequence [65]. In contrast, the clustering of embeddings in BERT has been associated with the representation of semantic information [63] (Fig. A2b). Thus, the underlying distribution ρ plays an important role.

3. Orthogonality and semi-orthogonality

A token’s query and key projections involve linear transformations $\iota : \mathbb{R}^d \rightarrow \mathbb{R}^{d_k}$. When there are multiple attention heads ($H > 1$), strict orthogonality is no longer preserved due to the division of the embedding dimension by H . Instead we have $\iota : \mathbb{R}^d \rightarrow \mathbb{R}^{d_H}$ where H is chosen so that $d \bmod H \equiv 0$ and the head dimension $d_H = d/H$ is thus an integer. Enforcing an orthogonal matrix \mathbf{W}_Q throughout training can be implemented in PyTorch via the `orthogonal` function. The projection for each attention head would be $\mathbf{W}_Q^{(i)} \mathbf{x} \in \mathbb{R}^{d_H}$, where $\mathbf{W}_Q^{(i)}$ is the submatrix $[\mathbf{W}_Q]_{(i-1)H+1:iH,:}$ for $i = 1, \dots, H - 1$. All the rows of \mathbf{W}_Q are orthogonal, and this does not make $\mathbf{W}_Q^{(i)} \in \mathbb{R}^{d_H \times d}$ semi-orthogonal from the left, i.e., $\mathbf{W}_Q^{(i)} \mathbf{x}$ no longer preserves the Euclidean distance for $\mathbf{x} \in \mathbb{R}^d$.

4. Continuous limits of the kernel construction

Here we outline a more general construction of the attention weights $\tilde{\mathbf{A}}$ in equation 14 encountered in diffusion maps [18]. Construct the diagonal matrix $D_{ii} = \sum_j \tilde{C}_{ij}$ and the new kernel $\mathbf{K}^{(a)}$

$$\tilde{\mathbf{C}}^{(a)} = \mathbf{D}^{-a} \tilde{\mathbf{C}} \mathbf{D}^{-a}. \quad (\text{A3})$$

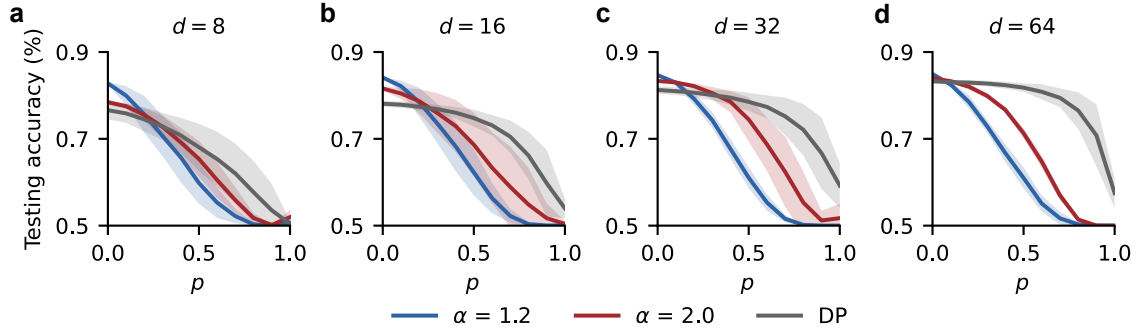


Fig. A3. Ablation of nodes from the attention graph. Testing accuracy after the randomly ablating nodes from the attention graph with probability p . Lines represent the mean across five trials for each network using $\mathbf{Q} \neq \mathbf{K}$. Shaded regions represent the standard deviation. **a** $d = 8$. **b** $d = 16$. **c** $d = 32$. **d** $d = 64$.

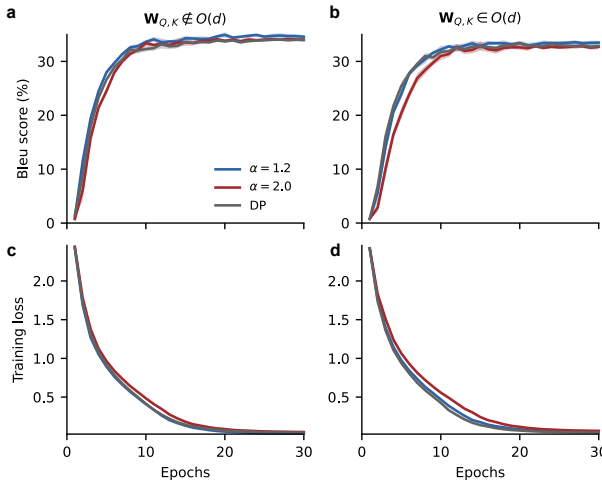


Fig. A4. Learning curves for machine translation. **a** Mean accuracy on the testing dataset across five trials for FNA ($\alpha = 1.2, 2$) and Transformer (DP) using $\mathbf{W}_{Q,K} \notin O(d)$. The shaded area represents a standard deviation. **b** Same as **a**, except using $\mathbf{W}_{Q,K} \in O(d)$. **c** Same as **a**, except showing the loss on the testing dataset. **d** Same as **c**, except using $\mathbf{W}_{Q,K} \in O(d)$.

After applying the weighted graph Laplacian normalization based on the parameter α to form the new kernel (equation A3), the alternative kernel is simply its row-normalization:

$$D_{ii}^{(a)} = \sum_j \tilde{C}_{ij}^{(a)}, \quad (A4)$$

$$\mathbf{A}^{(a)} = (\mathbf{D}^{(a)})^{-1} \tilde{\mathbf{C}}^{(a)} \equiv N_R(\tilde{\mathbf{C}}^{(a)}). \quad (A5)$$

The case of equation 14 is equivalent to $\mathbf{A}^{(0)}$ where we suppress the superscript for notation simplicity. In the limit of an infinite sequence $n \rightarrow \infty$, the summation of equation 13 can be written in the form of Monte Carlo integration:

$$\lim_{n \rightarrow \infty} \frac{1}{n} \sum_{i=1}^n A_{ij}^{(a)} = \int_{\mathcal{M}} k_{\varepsilon}^{(a)}(\mathbf{x}, \mathbf{y}) q(\mathbf{y}) d\text{vol}_{\mathbf{y}} \propto \rho(\mathbf{x}) + O(\varepsilon) \quad (A6)$$

where $O(\cdot)$ is the big-O notation.

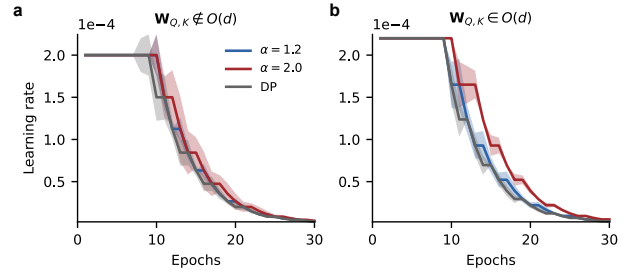


Fig. A5. Learning rates for machine translation. **a** Mean learning rate for the training process across five trials for FNA ($\alpha = 1.2, 2$) and Transformer (DP) using $\mathbf{W}_{Q,K} \notin O(d)$. The shaded area represents a standard deviation. **b** Same as **a**, except using $\mathbf{W}_{Q,K} \in O(d)$.

We list the continuous counterpart of the kernel construction in Section and the current section through integral representations.

1. Set a rotation-invariant kernel for all pairs of points $\mathbf{x}, \mathbf{y} \in \mathcal{M}$

$$\tilde{c}_{\varepsilon}(\mathbf{x}, \mathbf{y}) = \Phi\left(\frac{1}{\sqrt{\varepsilon}}d_g(\mathbf{x}, \mathbf{y})\right) \quad (A7)$$

2. Let

$$q_{\varepsilon}(\mathbf{x}) := \int k_{\varepsilon}(\mathbf{x}, \mathbf{y}) q(\mathbf{y}) d\mathbf{y} \quad (A8)$$

and the new kernel

$$\tilde{c}_{\varepsilon}^{(a)}(\mathbf{x}, \mathbf{y}) := \frac{\tilde{c}_{\varepsilon}(\mathbf{x}, \mathbf{y})}{q_{\varepsilon}(\mathbf{x})^a q_{\varepsilon}(\mathbf{y})^a}. \quad (A9)$$

Finally, apply the weighted graph Laplacian normalization to this kernel by setting

$$d_{\varepsilon}^{(a)}(\mathbf{x}) := \int_X k_{\varepsilon}^{(a)}(\mathbf{x}, \mathbf{y}) q(\mathbf{y}) d\mathbf{y} \quad (A10)$$

and by defining the anisotropic transition kernel

$$k_{\varepsilon}^{(a)}(\mathbf{x}, \mathbf{y}) := \frac{\tilde{c}_{\varepsilon}^{(a)}(\mathbf{x}, \mathbf{y})}{d_{\varepsilon}^{(a)}(\mathbf{x})}. \quad (A11)$$

The choice of normalization index a affects the operator limit of $k_\varepsilon^{(a)}$ as $\varepsilon \rightarrow 0$ (equation A3–A5). For $a = 2$, in the case of $a = 1$, the model removes the effects of ρ and thus becomes agnostic of the initial sampling distribution of the tokens/hidden states ρ . In our construction, the underlying manifold of the hidden states is known, making the embedding distribution ρ crucial. Therefore, we set $a = 0$ for FNA in equation 14.

5. Additional results for text classification

Here we show the results for the case of $\mathbf{Q} \neq \mathbf{K}$ (Fig. A3 in correspondence to Fig. 4 in the main text.

6. Additional results for machine translate

We display the training curves (Fig. A4) for machine translation in the main text corresponding to Table II.

Since the learning rate varies under the ReduceLROnPlateau scheme, we plot its evolution during training (Fig. A5).

[1] Vaswani, A., Shazeer, N., Parmar, N., Uszkoreit, J., Jones, L., Gomez, A.N., Kaiser, Ł., and Polosukhin, I. Attention is all you need. *Advances in Neural Information Processing Systems*, 30, 2017.

[2] Liu, Y., Ott, M., Goyal, N., Du, J., Joshi, M., Chen, D., Levy, O., Lewis, M., Zettlemoyer, L., and Stoyanov, V. RoBERTa: A robustly optimized BERT pretraining approach. *arXiv preprint arXiv:1907.11692*, 2019.

[3] Zhu, J., Xia, Y., Wu, L., He, D., Qin, T., Zhou, W., Li, H., and Liu, T.Y. Incorporating BERT into neural machine translation. *International Conference on Learning Representations*, 2020.

[4] Li, S., Jin, X., Xuan, Y., Zhou, X., Chen, W., Wang, Y.X., and Yan, X. Enhancing the locality and breaking the memory bottleneck of transformer on time series forecasting. *Advances in Neural Information Processing Systems*, 32, 2019.

[5] Zhou, T., Ma, Z., Wen, Q., Wang, X., Sun, L., and Jin, R. FED-former: Frequency enhanced decomposed transformer for long-term series forecasting. *International Conference on Machine Learning*, pages 27268–27286, 2022.

[6] Dosovitskiy, A. An image is worth 16x16 words: Transformers for image recognition at scale. *International Conference on Learning Representations*, 2021.

[7] Yang, J., Liu, Z., Xiao, S., Li, C., Lian, D., Agrawal, S., Singh, A., Sun, G., and Xie, X. Graphformers: GNN-nested transformers for representation learning on textual graph. *Advances in Neural Information Processing Systems*, 34:28798–28810, 2021.

[8] Lu, Y., Li, Z., He, D., Sun, Z., Dong, B., Qin, T., Wang, L., and Liu, T.Y. Understanding and improving transformer from a multi-particle dynamic system point of view. *International Conference on Learning Representations Workshop DeepDiffEq*, 2020.

[9] Sander, M.E., Ablin, P., Blondel, M., and Peyré, G. Sinkformers: Transformers with doubly stochastic attention. *International Conference on Artificial Intelligence and Statistics*, pages 3515–3530, 2022.

[10] Zaheer, M., Guruganesh, G., Dubey, K.A., Ainslie, J., Alberti, C., Ontanon, S., Pham, P., Ravula, A., Wang, Q., Yang, L., et al. Big bird: Transformers for longer sequences. *Advances in Neural Information Processing Systems*, 33:17283–17297, 2020.

[11] Beltagy, I., Peters, M.E., and Cohan, A. Longformer: The long-document transformer. *arXiv preprint arXiv:2004.05150*, 2020.

[12] Chen, G. and Gong, P. A spatiotemporal mechanism of visual attention: Superdiffusive motion and theta oscillations of neural population activity patterns. *Science Advances*, 8(16):eabl4995, 2022.

[13] Qi, Y. and Gong, P. Fractional neural sampling as a theory of spatiotemporal probabilistic computations in neural circuits. *Nature Communications*, 13(1):4572, 2022.

[14] Hassabis, D., Kumaran, D., Summerfield, C., and Botvinick, M. Neuroscience-inspired artificial intelligence. *Neuron*, 95(2):245–258, 2017.

[15] Zador, A., Escola, S., Richards, B., Ölveczky, B., Bengio, Y., Boahen, K., Botvinick, M., Chklovskii, D., Churchland, A., Clopath, C., DiCarlo, J., Ganguli, S., Hawkins, J., Kording, K., Koulakov, A., LeCun, Y., Lillicrap, T., Marblestone, A., Olshausen, B., Pouget, A., Savin, C., Sejnowski, T., Simoncelli, E., Solla, S., Sussillo, D., Tolias, A.S., and Tsao, D. Catalyzing next-generation artificial intelligence through neuroai. *Nature Communications*, 14(1), 2023.

[16] Lischke, A., Pang, G., Gulian, M., Song, F., Glusa, C., Zheng, X., Mao, Z., Cai, W., Meerschaert, M.M., Ainsworth, M., and Karniadakis, G.E. What is the fractional laplacian? A comparative review with new results. *Journal of Computational Physics*, 404:109009, 2020.

[17] Applebaum, D. *Lévy Processes and Stochastic Calculus*. Cambridge Studies in Advanced Mathematics. Cambridge University Press, 2 edition, 2009.

[18] Coifman, R.R. and Lafon, S. Diffusion maps. *Applied and Computational Harmonic Analysis*, 21(1):5–30, 2006. Special Issue: Diffusion Maps and Wavelets.

[19] Antil, H., Berry, T., and Harlim, J. Fractional diffusion maps. *Applied and Computational Harmonic Analysis*, 54:145–175, 2021.

[20] Elliott, D., Frank, S., Sima'an, K., and Specia, L. Multi30k: Multilingual english-german image descriptions. *Proceedings of the 5th Workshop on Vision and Language*, pages 70–74, 2016.

[21] Bahdanau, D., Cho, K., and Bengio, Y. Neural machine translation by jointly learning to align and translate. *International Conference on Learning Representations*, 2015.

[22] Lin, T., Wang, Y., Liu, X., and Qiu, X. A survey of transformers. *AI Open*, 3:111–132, 2022.

[23] Vuckovic, J., Baratin, A., and Combes, R.T.d. A mathematical theory of attention. *arXiv preprint arXiv:2007.02876*, 2020.

[24] Vuckovic, J., Baratin, A., and Combes, R.T.d. On the regularity of attention. *arXiv preprint arXiv:2102.05628*, 2021.

[25] Geshkovski, B., Letrouit, C., Polyanskiy, Y., and Rigollet, P. The emergence of clusters in self-attention dynamics. *Advances in Neural Information Processing Systems*, 36:57026–57037, 2023.

[26] Dong, Y., Cordonnier, J.B., and Loukas, A. Attention is not all you need: Pure attention loses rank doubly exponentially with depth. *International Conference on Machine Learning*, pages 2793–2803, 2021.

[27] Chen, R.T., Rubanova, Y., Bettencourt, J., and Duvenaud, D.K. Neural ordinary differential equations. *Advances in Neural Information Processing Systems*, 31, 2018.

[28] Renardy, M. and Rogers, R.C. *An Introduction to Partial Differential Equations*. Texts in Applied Mathematics, 13. Springer New York, New York, NY, 2nd ed. 2004. edition, 2004. ISBN 1-280-18891-X.

[29] Koubbi, H., Boussard, M., and Hernandez, L. The impact of LoRA on the emergence of clusters in transformers. *arXiv preprint arXiv:2402.15415*, 2024.

[30] Brown, T., Mann, B., Ryder, N., Subbiah, M., Kaplan, J.D., Dhariwal, P., Neelakantan, A., Shyam, P., Sastry, G., Askell, A., et al. Language models are few-shot learners. *Advances in Neural Information Processing Systems*, 33:1877–1901, 2020.

[31] Kwaśnicki, M. Ten equivalent definitions of the fractional laplace operator. *Fractional Calculus and Applied Analysis*, 20(1):7–51, 2017.

[32] Grigor, A. and Kumagai, T. On the dichotomy in the heat kernel two sided estimates. *Analysis on Graphs and its Applications (P. Exner et al.(eds.)), Proc. of Symposia in Pure Math*, 77, 01 2008.

[33] Viswanathan, G.M., Buldyrev, S.V., Havlin, S., da Luz, M.G., Raposo, E.P., and Stanley, H.E. Optimizing the success of random searches. *Nature*, 401(6756):911–914, 1999.

[34] Klages, R., Radons, G., and Sokolov, I.M. *Anomalous transport*. Wiley Online Library, 2008.

[35] Kim, H., Papamakarios, G., and Mnih, A. The Lipschitz constant of self-attention. *International Conference on Machine Learning*, pages 5562–5571, 2021.

[36] Lezcano Casado, M. Trivializations for gradient-based optimization on manifolds. *Advances in Neural Information Processing Systems*, 32, 2019.

[37] Sengupta, A., Akhtar, M., and Chakraborty, T. Manifold-preserving transformers are effective for short-long range encoding. *Findings of the Association for Computational Linguistics: EMNLP 2023*, pages 3533–3549, 2023.

[38] Chen, Y., Zeng, Q., Ji, H., and Yang, Y. Skyformer: Remodel self-attention with Gaussian kernel and Nyström method. *Advances in Neural Information Processing Systems*, 34:2122–2135, 2021.

[39] Nadler, B., Lafon, S., Coifman, R., and Kevrekidis, I.G. Diffusion maps-a probabilistic interpretation for spectral embedding and clustering algorithms. In *Principal manifolds for data visualization and dimension reduction*, pages 238–260. Springer, 2008.

[40] Weyl, H. Das asymptotische Verteilungsgesetz der Eigenwerte linearer partieller Differentialgleichungen (mit einer Anwendung auf die Theorie der Hohlraumstrahlung). *Mathematische Annalen*, 71(4):441–479, 1912.

[41] Bahri, Y., Kadmon, J., Pennington, J., Schoenholz, S.S., Sohl-Dickstein, J., and Ganguli, S. Statistical mechanics of deep learning. *Annual Review of Condensed Matter Physics*, 11(1): 501–528, 2020.

[42] Maas, A., Daly, R.E., Pham, P.T., Huang, D., Ng, A.Y., and Potts, C. Learning word vectors for sentiment analysis. *Proceedings of the 49th Annual Meeting of the Association for Computational Linguistics: Human Language Technologies*, pages 142–150, 2011.

[43] Dao, T., Fu, D., Ermon, S., Rudra, A., and Ré, C. FlashAttention: Fast and memory-efficient exact attention with IO-awareness. *Advances in Neural Information Processing Systems*, 35:16344–16359, 2022.

[44] Krizhevsky, A., Hinton, G., et al. Learning multiple layers of features from tiny images, 2009.

[45] Papineni, K., Roukos, S., Ward, T., and Zhu, W.J. Bleu: a method for automatic evaluation of machine translation. *Proceedings of the 40th Annual Meeting of the Association for Computational Linguistics*, pages 311–318, 2002.

[46] Xiong, Y., Zeng, Z., Chakraborty, R., Tan, M., Fung, G., Li, Y., and Singh, V. Nyströmformer: A Nyström-based algorithm for approximating self-attention. *Proceedings of the AAAI Conference on Artificial Intelligence*, 35(16):14138–14148, 2021.

[47] Miyato, T., Kataoka, T., Koyama, M., and Yoshida, Y. Spectral normalization for generative adversarial networks. In *International Conference on Learning Representations*, 2018.

[48] Behrmann, J., Grathwohl, W., Chen, R.T.Q., Duvenaud, D., and Jacobsen, J.H. Invertible residual networks. *International Conference on Machine Learning*, 97:573–582, 2019.

[49] Chen, R.T.Q., Behrmann, J., Duvenaud, D.K., and Jacobsen, J.H. Residual flows for invertible generative modeling. In Wallach, H., Larochelle, H., Beygelzimer, A., d’Alché-Buc, F., Fox, E., and Garnett, R., editors, *Advances in Neural Information Processing Systems*, volume 32. Curran Associates, Inc., 2019.

[50] Wang, X., Girshick, R., Gupta, A., and He, K. Non-local neural networks. *Proceedings of the IEEE Conference on Computer Vision and Pattern Recognition*, pages 7794–7803, 2018.

[51] Munn, B. and Gong, P. Critical dynamics of natural time-varying images. *Physical Review Letters*, 121(5):058101, 2018.

[52] Ruderman, D.L. and Bialek, W. Statistics of natural images: Scaling in the woods. *Physical Review Letters*, 73(6):814–817, August 1994.

[53] Field, D.J. Relations between the statistics of natural images and the response properties of cortical cells. *J. Opt. Soc. Am. A*, 4(12):2379–2394, 1987.

[54] Alabdulmohsin, I.M., Tran, V., and Dehghani, M. Fractal patterns may illuminate the success of next-token prediction. *Advances in Neural Information Processing Systems*, 37:112864–112888, 2024.

[55] Gilden, D.L., Thornton, T., and Mallon, M.W. 1/f noise in human cognition. *Science*, 267(5205):1837–1839, 1995.

[56] Kello, C.T., Brown, G.D., Ferrer-i Cancho, R., Holden, J.G., Linkenkaer-Hansen, K., Rhodes, T., and Van Orden, G.C. Scaling laws in cognitive sciences. *Trends in Cognitive Sciences*, 14(5):223–232, 2010.

[57] He, B.J. Scale-free brain activity: past, present, and future. *Trends in Cognitive Sciences*, 18(9):480–487, September 2014.

[58] Nolan, J.P. Basic properties of univariate stable distributions. In *Univariate Stable Distributions: Models for Heavy Tailed Data*, pages 1–23. Springer, 2020.

[59] Samorodnitsky, G. and Taqqu, M.S. *Stable non-Gaussian random processes: stochastic models with infinite variance*, volume 1. CRC press, 1994.

[60] Evans, L., Cameron, M.K., and Tiwary, P. Computing committee via Mahalanobis diffusion maps with enhanced sampling data. *The Journal of Chemical Physics*, 157(21), 2022.

[61] Kingma, D.P. and Ba, J. Adam: A method for stochastic optimization. *International Conference on Learning Representations*, 2015.

[62] Lan, Z., Chen, M., Goodman, S., Gimpel, K., Sharma, P., and Soricut, R. ALBERT: A lite BERT for self-supervised learning of language representations. *International Conference on Learning Representations*, 2020.

[63] Devlin, J., Chang, M.W., Lee, K., and Toutanova, K. BERT: Pre-training of deep bidirectional transformers for language understanding. *Proceedings of the 2019 Conference of the North American Chapter of the Association for Computational Linguistics: Human Language Technologies, Volume 1 (Long and Short Papers)*, pages 4171–4186, 2019.

[64] Radford, A., Wu, J., Child, R., Luan, D., Amodei, D., Sutskever, I., et al. Language models are unsupervised multitask learners. *OpenAI blog*, 1(8):9, 2019.

[65] Cai, X., Huang, J., Bian, Y., and Church, K. Isotropy in the contextual embedding space: Clusters and manifolds. *International Conference on Learning Representations*, 2021.

Acknowledgments This work was supported by the Australian Research Council (grant no. DP160104368).

Author Contributions C.K.Q, A.L. and P.G. designed the study, performed the research and wrote the paper.